Cell Reports

Article

Mutation-induced LZTR1 polymerization provokes cardiac pathology in recessive Noonan syndrome

Graphical abstract

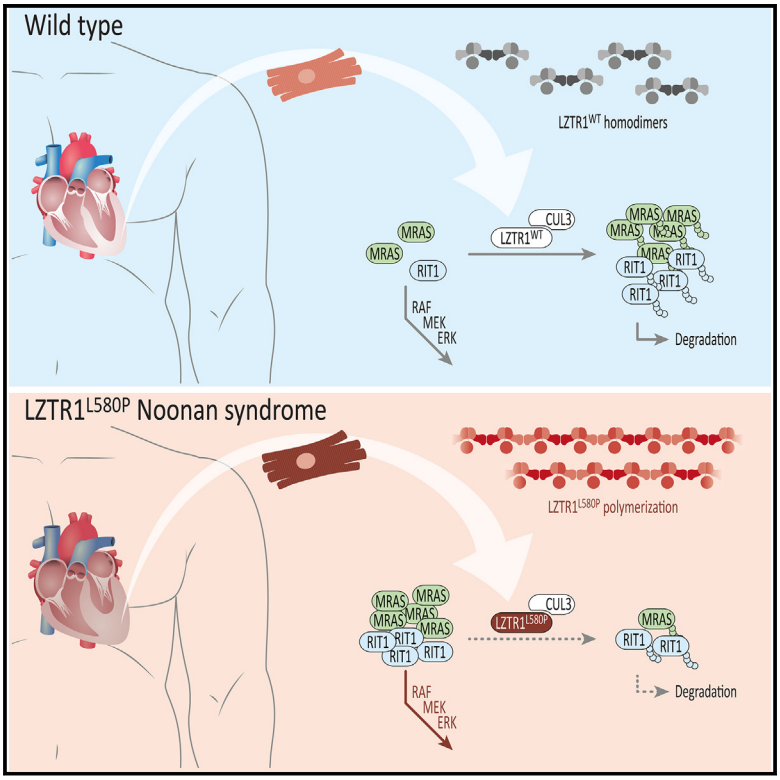

Highlights

- LZTR1^{L580P} in homozygosity is causative for Noonan syndrome and hypertrophic cardiomyopathy
- LZTR1^{L580P} fosters assembly of LZTR1 polymers, resulting in complex dysfunction
- Pathological LZTR1 results in impaired RAS GTPase degradation, causing cellular hypertrophy
- CRISPR correction of one allele is sufficient to normalize cardiac disease phenotype

Authors

Alexandra Viktoria Busley, Óscar Gutiérrez-Gutiérrez, Elke Hammer, ..., Mohammad Reza Ahmadian, Bernd Wollnik, Lukas Cyganek

Correspondence

lukas.cyganek@gwdg.de

In brief

Using patient-specific and CRISPR-Cas9-corrected iPSC cardiomyocytes, Busley et al. describe an *LZTR1^{L580P}*-specific disease mechanism provoking Noonan syndrome-associated cardiac hypertrophy. Mutation-induced polymerization of LZTR1 complexes results in the accumulation of RAS GTPases, leading to molecular and cellular impairments associated with cardiac hypertrophy, whereas CRISPR correction of the missense variant rescues the disease phenotype.

Busley et al., 2024, Cell Reports *43*, 114448
July 23, 2024
https://doi.org/10.1016/j.celrep.2024.114448

CellPress

Cell Reports

CellPress
OPEN ACCESS

Article

Mutation-induced LZTR1 polymerization provokes cardiac pathology in recessive Noonan syndrome

Alexandra Viktoria Busley,[1,2,4,20] Óscar Gutiérrez-Gutiérrez,[1,2,20] Elke Hammer,[3,5] Fabian Koitka,[1,2,4] Amin Mirzaiebadizi,[6] Martin Steinegger,[7] Constantin Pape,[4,8] Linda Böhmer,[1] Henning Schroeder,[9] Mandy Kleinsorge,[1,2] Melanie Engler,[10] Ion Cristian Cirstea,[10] Lothar Gremer,[11,12] Dieter Willbold,[11,12] Janine Altmüller,[13,14] Felix Marbach,[15,16] Gerd Hasenfuss,[1,2,4] Wolfram-Hubertus Zimmermann,[2,4,17,18] Mohammad Reza Ahmadian,[6] Bernd Wollnik,[2,4,19] and Lukas Cyganek[1,2,4,18,21,*]

[1]Stem Cell Unit, Clinic for Cardiology and Pneumology, University Medical Center Göttingen, Göttingen, Germany
[2]DZHK (German Center for Cardiovascular Research), Göttingen, Germany
[3]DZHK (German Center for Cardiovascular Research), Greifswald, Germany
[4]Cluster of Excellence "Multiscale Bioimaging: from Molecular Machines to Networks of Excitable Cells" (MBExC), University of Göttingen, Göttingen, Germany
[5]Interfaculty Institute of Genetics and Functional Genomics, University Medicine Greifswald, Greifswald, Germany
[6]Institute of Biochemistry and Molecular Biology II, Medical Faculty and University Hospital Düsseldorf, Heinrich Heine University Düsseldorf, Düsseldorf, Germany
[7]School of Biological Sciences, Seoul National University, Seoul, South Korea
[8]Institute of Computer Science, Georg-August University Göttingen, Göttingen, Germany
[9]NMR Signal Enhancement Group, Max Planck Institute for Multidisciplinary Sciences, Göttingen, Germany
[10]Institute of Applied Physiology, University of Ulm, Ulm, Germany
[11]Institute of Physical Biology, Heinrich Heine University Düsseldorf, Düsseldorf, Germany
[12]Institute of Biological Information Processing, Structural Biochemistry (IBI-7), Forschungszentrum Jülich GmbH, Jülich, Germany
[13]Cologne Center for Genomics, University of Cologne, Faculty of Medicine, and University Hospital Cologne, Cologne, Germany
[14]Genomics Platform, Berlin Institute for Medical Systems Biology, Max Delbrück Center for Molecular Medicine–Berlin, Berlin, Germany
[15]Institute of Human Genetics, University Hospital Cologne, Cologne, Germany
[16]Institute of Human Genetics, Heidelberg University, Heidelberg, Germany
[17]Institute of Pharmacology and Toxicology, University Medical Center Göttingen, Göttingen, Germany
[18]Translational Neuroinflammation and Automated Microscopy, Fraunhofer Institute for Translational Medicine and Pharmacology ITMP, Göttingen, Germany
[19]Institute of Human Genetics, University Medical Center Göttingen, Göttingen, Germany
[20]These authors contributed equally
[21]Lead contact
*Correspondence: lukas.cyganek@gwdg.de
https://doi.org/10.1016/j.celrep.2024.114448

SUMMARY

Noonan syndrome patients harboring causative variants in *LZTR1* are particularly at risk to develop severe and early-onset hypertrophic cardiomyopathy. In this study, we investigate the mechanistic consequences of a homozygous variant *LZTR1*^{L580P} by using patient-specific and CRISPR-Cas9-corrected induced pluripotent stem cell (iPSC) cardiomyocytes. Molecular, cellular, and functional phenotyping in combination with *in silico* prediction identify an *LZTR1*^{L580P}-specific disease mechanism provoking cardiac hypertrophy. The variant is predicted to alter the binding affinity of the dimerization domains facilitating the formation of linear LZTR1 polymers. LZTR1 complex dysfunction results in the accumulation of RAS GTPases, thereby provoking global pathological changes of the proteomic landscape ultimately leading to cellular hypertrophy. Furthermore, our data show that cardiomyocyte-specific MRAS degradation is mediated by LZTR1 via non-proteasomal pathways, whereas RIT1 degradation is mediated by both LZTR1-dependent and LZTR1-independent pathways. Uni- or biallelic genetic correction of the *LZTR1*^{L580P} missense variant rescues the molecular and cellular disease phenotype, providing proof of concept for CRISPR-based therapies.

INTRODUCTION

Noonan syndrome (NS) is a multi-systemic developmental disorder with a broad spectrum of symptoms and varying degrees of disease severity. Common clinical symptoms range from intellectual disability to facial dysmorphisms, webbed neck, skeletal deformities, short stature, and, in many cases, congenital heart disease.[1] With a prevalence of approximately 1 in 1,000–2,500

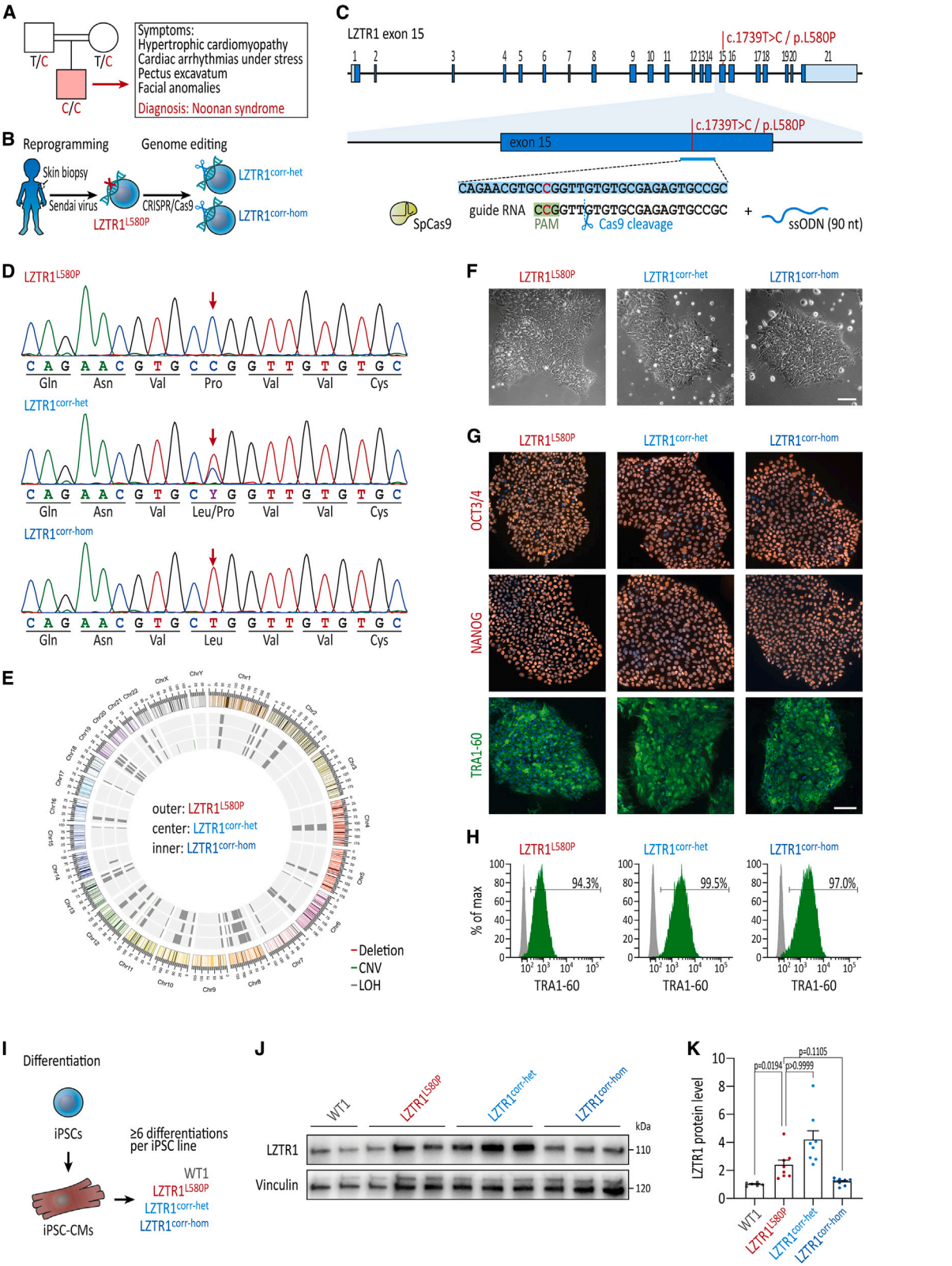

(legend on next page)

live births, NS is considered the most common monogenic disease associated with congenital heart defects and early-onset hypertrophic cardiomyopathy (HCM).[2] Young NS patients diagnosed with HCM are more prone to develop heart failure accompanied by a poor late survival.[3,4] Like other phenotypically overlapping syndromes classified as RASopathies, NS is caused by variants in RAS-mitogen-activated protein kinase (MAPK)-associated genes, all typically leading to an increase in signaling transduction.[5] Patients harboring causative gene variants in *RAF1*, *HRAS*, *RIT1*, and *LZTR1* are particularly at risk to develop severe and early-onset HCM.[6,7]

Recent studies by others and our group have identified the role of LZTR1 within the RAS-MAPK signaling cascade as a negative regulator of signaling activity. *LZTR1* encodes an adapter protein of the cullin 3 ubiquitin ligase complex by selectively targeting RAS proteins as substrates for degradation. *LZTR1* deficiency, caused by truncating or missense variants, results in an accumulation of the RAS protein pool and, as a consequence, in RAS-MAPK signaling hyperactivity.[8–10] Whereas dominant *LZTR1* variants generally cluster in the Kelch motif perturbing RAS binding to the ubiquitination complex,[11] the mechanistic consequences of recessive *LZTR1* missense variants, which are distributed over the entire protein, are not understood.

Human induced pluripotent stem cell-derived cardiomyocytes (iPSC-CMs) generated from patients with inherited forms of cardiomyopathies offer a platform to study the disease mechanisms in physiologically relevant cells and tissues.[12,13] A few RASopathy-linked iPSC-CM models have been described, including for variants in *PTPN11*, *RAF1*, *BRAF*, and *MRAS*.[14–17] With this in mind, we recently added additional information as to the role of *LZTR1*-truncating variants in NS pathophysiology.[10,18] In the present study, we investigated the functional consequences of a recessive missense variant *LZTR1*^{L580P} by utilizing patient-derived and CRISPR-corrected iPSC-CMs. We could show that *LZTR1*^{L580P} in homozygosity results in aberrant polymerization causing LZTR1 dysfunction, an increase in RAS guanosine triphosphatase (GTPase) levels, and cellular hypertrophy. Furthermore, genetic correction of the missense variant by CRISPR-Cas9 rescued the cellular phenotype, thereby providing proof of concept for future personalized CRISPR-based therapies.

RESULTS

LZTR1^{L580P} is causative for recessive NS

A 17-year-old male patient with HCM, stress-induced cardiac arrhythmias, pectus excavatum, and facial anomalies was referred to our clinic, and, based on the combination of symptoms, was diagnosed with NS (Figure 1A; Table S1). The patient was born to a consanguineous couple, and both parents showed neither apparent clinical symptoms nor distinctive NS-specific features. Whole-exome sequencing detected one highly suspicious homozygous variant in *LZTR1* (GenBank: NM_006767), c.1739T>C, leading to the substitution of an evolutionary conserved leucine at amino acid position 580 by proline (p.L580P). Both parents were heterozygous carriers, and the variant was not present in any current database of human genetic variations, including the >250,000 alleles of the Genome Aggregation Database (gnomAD).

To elucidate the molecular and functional consequences of the *LZTR1*^{L580P} missense variant, we generated iPSCs from the patient's skin fibroblasts using integration-free reprogramming methods and subsequently utilized CRISPR-Cas9 genome editing to engineer gene variant-corrected iPSC lines (Figure 1B). For genetic correction of the patient-specific iPSCs, the CRISPR guide RNA was designed to specifically target the mutated sequence in exon 15 of the *LZTR1* gene. Furthermore, the ribonucleoprotein-based CRISPR-Cas9 complex was combined with a single-stranded oligonucleotide serving as template for homology-directed repair (Figure 1C). Upon transfection, cells were singularized and individual clones were screened for successful editing to identify heterozygous corrected as well as homozygous corrected iPSC clones, LZTR1$^{corr\text{-}het}$ and LZTR1$^{corr\text{-}hom}$, respectively (Figure 1D). Molecular karyotyping of the edited iPSC clones confirmed chromosomal stability after genome editing and passaging (Figure 1E). As expected for individuals born from consanguineous parents, both patient-specific and CRISPR-corrected iPSCs demonstrated a noticeable reduction

Figure 1. Generation of patient-specific and CRISPR-corrected iPSCs

(A) Pedigree of the consanguineous family with healthy parents and the son affected by recessive NS harboring the *LZTR1* variant (c.1739T>C/p.L580P) in homozygosity.

(B) Generation of patient-specific iPSCs by reprogramming of patient's skin fibroblasts via integration-free Sendai virus and genetic correction of the missense variant by CRISPR-Cas9.

(C) Depiction of the genome editing approach for correction of the missense variant in *LZTR1* exon 15.

(D) Sanger sequencing of the patient-derived iPSCs (LZTR1^{L580P}) and the CRISPR-Cas9-edited heterozygous corrected (LZTR1$^{corr\text{-}het}$) and homozygous corrected (LZTR1$^{corr\text{-}hom}$) iPSCs.

(E) Molecular karyotyping demonstrated a high percentage of loss of heterozygosity (LOH) because of consanguinity as well as chromosomal stability of iPSCs after genome editing. CNV, copy number variation.

(F) Patient-specific and CRISPR-corrected iPSCs showed a typical human stem cell-like morphology; scale bar: 100 μm.

(G) Expression of key pluripotency markers OCT3/4, NANOG, and TRA-1-60 in the generated iPSC lines was assessed by immunocytochemistry; nuclei were counter-stained with Hoechst 33342 (blue); scale bar: 100 μm.

(H) Flow cytometry analysis of pluripotency marker TRA-1-60 detected homogeneous populations of pluripotent cells in generated iPSC lines. Gray peaks represent the negative controls.

(I) Differentiation of WT, patient-specific, and CRISPR-corrected iPSCs into iPSC-CMs.

(J) Representative blot of endogenous LZTR1 levels in iPSC-CMs at day 60 of differentiation, assessed by western blot; vinculin served as loading control; $n = 3$ individual differentiations per iPSC line.

(K) Quantitative analysis of western blots for LZTR1; data were normalized to total protein and to the corresponding WT samples on each membrane; $n = 6–8$ independent differentiations per iPSC line. Data were analyzed by non-parametric Kruskal-Wallis test with Dunn correction and are presented as mean ± SEM (K).

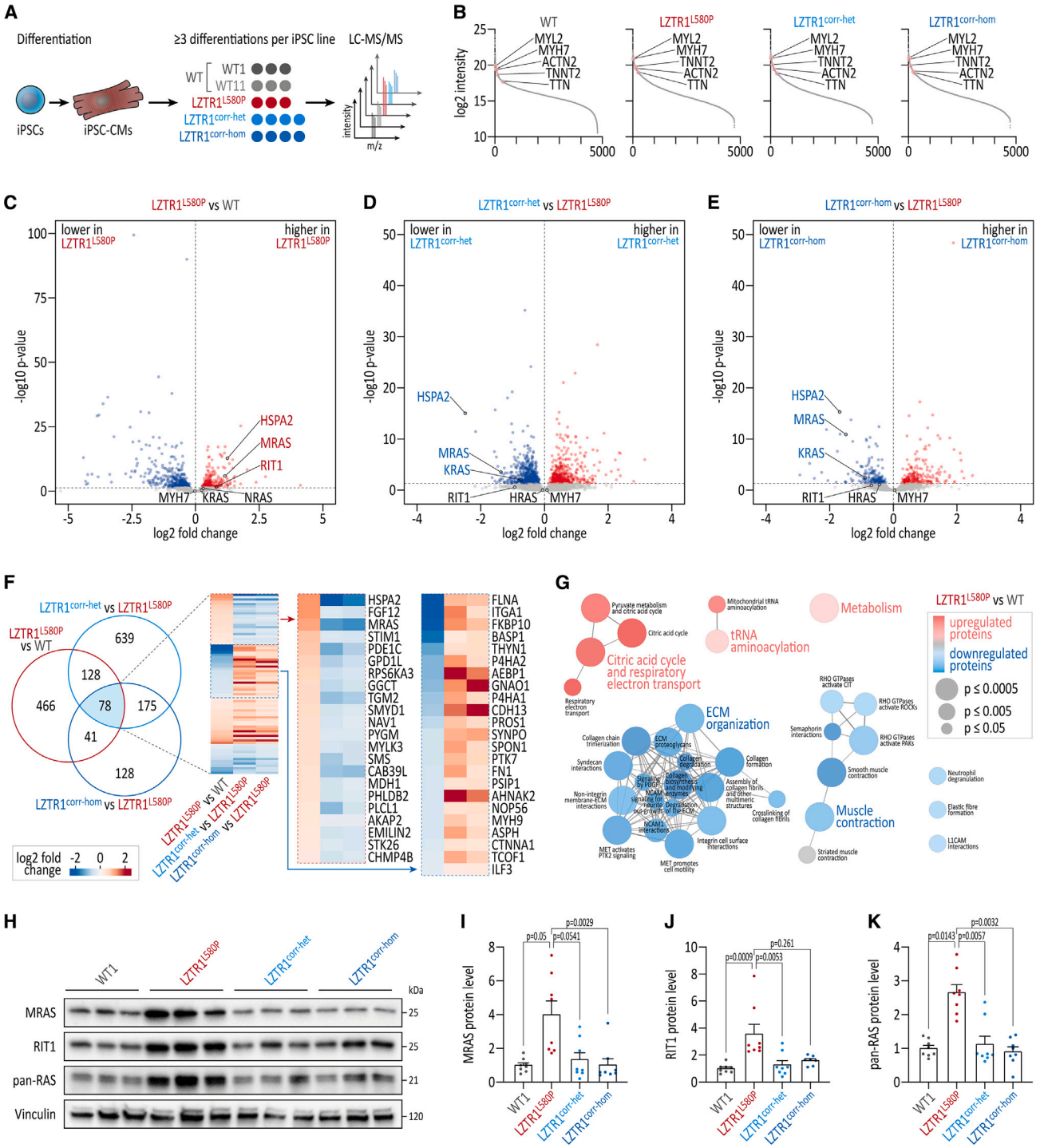

Figure 2. Homozygous *LZTR1*^{L580P} causes accumulation of RAS GTPases

(A) Two WT, the patient-specific, and the 2 CRISPR-corrected iPSC lines were differentiated into ventricular iPSC-CMs and analyzed by quantitative global proteomics via liquid chromatography-tandem mass spectrometry at day 60 of differentiation; n = 3–4 individual differentiations per iPSC line.

(B) Over 4,700 proteins were present in the individual proteomic samples, all showing comparable high abundance of cardiac markers myosin heavy-chain β (*MHY7*), cardiac troponin T (*TNNT2*), α-actinin (*ACTN2*), titin (*TTN*), and ventricular-specific MLC2V (*MYL2*).

(C–E) Volcano plots comparing patient's versus WT iPSC-CMs (C; LZTR1^{L580P} versus WT), heterozygous corrected versus non-corrected iPSC-CMs (D; LZTR1$^{corr\text{-}het}$ versus LZTR1^{L580P}), and homozygous corrected versus non-corrected iPSC-CMs (E; LZTR1$^{corr\text{-}hom}$ versus LZTR1^{L580P}) detected high abundance of RAS GTPases in patient samples.

(legend continued on next page)

of the overall heterozygosity. In addition, sequencing detected no obvious off-target modifications by genome editing (Figure S1). Subsequently, patient-derived and CRISPR-corrected iPSCs were verified for pluripotency (Figures 1F–1H). In addition to the patient-derived iPSC lines, iPSC lines from two unrelated healthy male donors, namely WT1 and WT11, were used as wild-type (WT) controls in this study.

At first, we aimed to determine whether the LZTR1^{L580P} protein remains stably expressed or is rapidly degraded after protein translation. LZTR1 proteins were robustly detected by western blot in differentiated iPSC-CMs (Figures 1I–1K). Interestingly, significantly higher LZTR1 protein levels were present in the patient-specific and the heterozygous corrected iPSC-CMs compared to WT and homozygous corrected cultures, suggesting an accumulation of the mutant LZTR1^{L580P} proteins.

Homozygous LZTR1^{L580P} causes accumulation of RAS GTPases

To investigate the impact of the identified homozygous *LZTR1*^{L580P} missense variant on the molecular mechanisms contributing to left ventricular hypertrophy, patient-specific, heterozygous and homozygous corrected, and two individual WT iPSC lines were differentiated into functional ventricular-like iPSC-CMs in feeder-free culture conditions,[19] and on day 60 of differentiation, subjected to unbiased proteome analyses (Figure 2A). We identified more than 4,700 proteins in the samples from the individual groups. All samples showed a comparably high abundance of prominent cardiac markers *MHY7*, *TNNT2*, *ACTN2*, and *TTN*, and ventricular-specific *MYL2*, indicating equal cardiomyocyte content in the different cultures (Figure 2B). By comparing the proteome profiles of LZTR1^{L580P} and WT iPSC-CMs, we identified enhanced abundance of the RAS family members muscle RAS oncogene homolog (MRAS) and RIT1 in the patient's iPSC-CMs (Figure 2C). This finding is in agreement with our previous observation in *LZTR1*-truncating variant carriers[10] and confirms the pivotal role of LZTR1 in targeting RAS GTPases for LZTR1-cullin 3 ubiquitin ligase complex-mediated ubiquitination and degradation.[8,9] Furthermore, it highlights that *LZTR1*^{L580P} results in protein loss of function, causing an accumulation of RAS proteins in the cells, which provides molecular evidence for the causative nature of the missense variant. Strikingly, protein levels of the RAS GTPases were normalized in both the heterozygous and the homozygous corrected iPSC-CMs, confirming that only one functional *LZTR1* allele is sufficient to regulate the protein pool of RAS GTPases in cardiomyocytes (Figures 2D and 2E). As anticipated, transcriptome analyses showed similar mRNA expression levels of RAS GTPases in the patient's and CRISPR-corrected iPSC lines, indicating a post-translational cause for the higher abundance of RAS proteins in LZTR1^{L580P} cultures (Figure S2). In contrast, the significantly elevated protein levels of the protein quality control-associated heat shock-related 70-kDa protein 2 (*HSPA2*) in the patient's cells in comparison to the WT and CRISPR-corrected cells were related to the upregulation of gene expression, suggesting that HSPA2 is not directly targeted by LZTR1 for degradation.

To assess the correlation of proteomic signatures with *LZTR1* deficiency, we performed a comparative analysis of (1) LZTR1^{L580P} versus WT, (2) LZTR1$^{corr\text{-}het}$ versus LZTR1^{L580P}, and (3) LZTR1$^{corr\text{-}hom}$ versus LZTR1^{L580P}. We found 78 proteins being differentially regulated in all 3 datasets (Figure 2F). Here, a profound subset of proteins that were significantly higher abundant in the patient's cells, such as the MAPK-activated protein kinase RPS6KA3, were normalized after heterozygous and homozygous CRISPR correction of the pathological *LZTR1* variant. Vice versa, numerous downregulated proteins in the patient samples were found to be elevated in the gene-edited iPSC-CMs. We performed a Reactome pathway enrichment analysis to detect dysregulated pathways and/or biological processes associated with *LZTR1*^{L580P}. Differentially abundant proteins in patient-derived samples were enriched in critical cardiac-related biological processes, such as muscle contraction and extracellular matrix organization, as well as in cellular routes associated with metabolism (Figure 2G). Consistent with the proteomic data, western blot analysis confirmed the strong accumulation of MRAS, RIT1, and the classical RAS GTPases (HRAS, KRAS, and NRAS; detected by pan-RAS) in the LZTR1^{L580P} cultures, and illustrated a normalization of RAS levels in the CRISPR-corrected isogenic iPSC-CMs to WT control levels (Figures 2H–2K).

Collectively, these data demonstrate that the missense variant *LZTR1*^{L580P} in homozygosity resulted in protein loss of function, causing an accumulation of RAS GTPases as the critical underlying disease mechanism in cardiomyocytes from the NS patient, and with this, correction of the homozygous missense variant on at least one allele normalized the molecular pathology.

Homozygous LZTR1^{L580P} does not induce strong ERK hyperactivity

To explore the impact of RAS GTPase accumulation on RAS-MAPK signaling activity, we used an ERK kinase translocation reporter (ERK-KTR) to measure ERK signaling dynamics in live cells.[20] Patient-specific, heterozygous and homozygous corrected, and WT iPSC-CMs were efficiently transduced with the ERK-KTR lentivirus, and the activity of ERK was analyzed at day 60 of differentiation by measuring the ratio of cytosolic (corresponding to active ERK) to nuclear (corresponding to inactive ERK) fluorescent signals (Figures 3A and 3B). The specificity of the ERK biosensor was confirmed by a selective response to MEK inhibition, whereas no change in ERK biosensor activity

(F) Comparison of differentially abundant proteins between the 3 datasets identified an overlap of 78 proteins, many of which showed opposite abundance in patient's versus CRISPR-corrected iPSC-CMs.
(G) Reactome pathway enrichment analysis of differentially abundant proteins in LZTR1^{L580P} versus WT displayed dysregulation of cardiac-related processes.
(H) Representative blots of RAS GTPase levels in iPSC-CMs at day 60 of differentiation, assessed by western blot; vinculin served as loading control; $n = 3$ individual differentiations per iPSC line.
(I–K) Quantitative analysis of western blots for MRAS (I), RIT1 (J), and pan-RAS recognizing HRAS, KRAS, and NRAS (K); data were normalized to total protein and to the corresponding WT samples on each membrane; $n = 8$ independent differentiations per iPSC line. Data were analyzed by non-parametric Kruskal-Wallis test with Dunn correction and are presented as mean ± SEM (I–K).

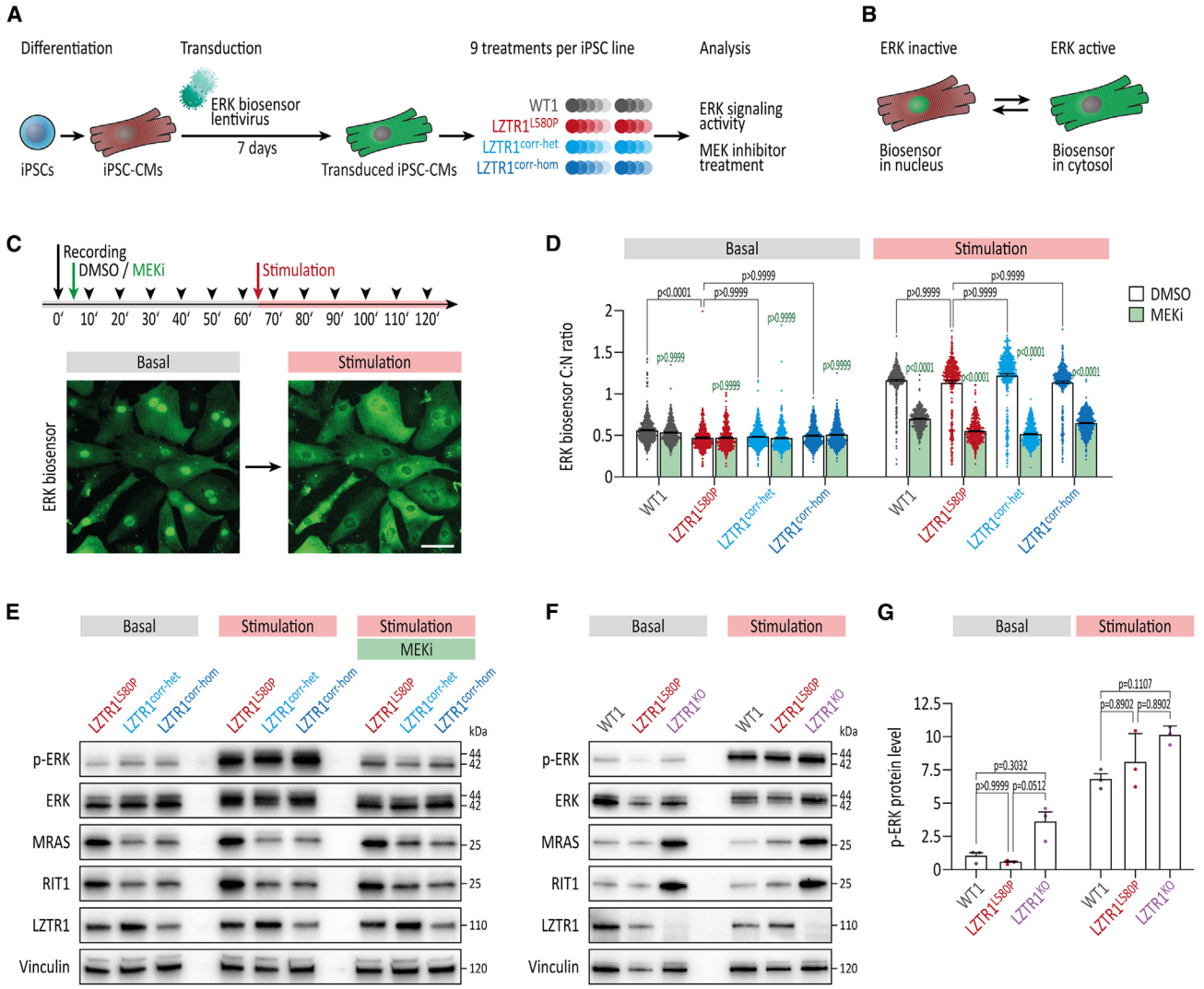

Figure 3. Homozygous *LZTR1*^{L580P} does not induce strong ERK hyperactivity

(A) WT, the patient-specific, and the 2 CRISPR-corrected iPSC lines were differentiated into ventricular iPSC-CMs and transduced around day 50 of differentiation with lentivirus containing an ERK kinase translocation reporter (ERK-KTR) to measure ERK signaling dynamics in real time.

(B) ERK activity was analyzed by measuring the ratio of cytosolic (corresponding to active ERK) to nuclear (corresponding to inactive ERK) fluorescent signals.

(C) Biosensor-transduced iPSC-CMs were treated with MEKi trametinib or with DMSO for 60 min, before stimulation with serum for another 60 min, and imaged every 10 min.

(D) Quantitative analysis of ERK biosensor cytosol:nucleus (C:N) ratio under basal conditions (60 min after MEKi/DMSO treatment) and 20 min after stimulation; $n = 2$ independent differentiations per iPSC line, with $n = 4–5$ individual wells per condition.

(E) Representative blots of p-ERK, ERK, MRAS, RIT1, and LZTR1 levels in iPSC-CMs at day 60 of differentiation under basal conditions and 30 min after stimulation with and without pre-treatment with MEKi, assessed by western blot; vinculin served as loading control.

(F) Representative blots of p-ERK, ERK, MRAS, RIT1, and LZTR1 levels in iPSC-CMs at day 60 of differentiation under basal conditions and 30 min after stimulation, assessed by western blot; vinculin served as loading control.

(G) Quantitative analysis of western blots for p-ERK protein levels; data were normalized to total protein and to the corresponding WT samples on each membrane; $n = 3$ independent differentiations per iPSC line.

Data were analyzed by non-parametric Kruskal-Wallis test with Dunn correction and are presented as mean ± SEM (D and G).

was observed when cells were treated with an inhibitor of the JNK pathway (Figure S3). Biosensor-transduced iPSC-CM cultures were treated with the MEK inhibitor (MEKi) trametinib or with DMSO for 60 min, before stimulation with fetal bovine serum for another 60 min, and imaged every 10 min (Figures 3C and S3). Under basal conditions, an equally low level of ERK activity was observed across all iPSC lines (Figure 3D). As expected, a strong increase in ERK activity was detected upon stimulation of the cells, while MEK inhibition was effective in normalizing ERK signaling activity (Figure 3D). The results of the imaging-based approach were confirmed by western blot analysis of uncorrected and CRISPR-corrected iPSC-CMs (Figure 3E).

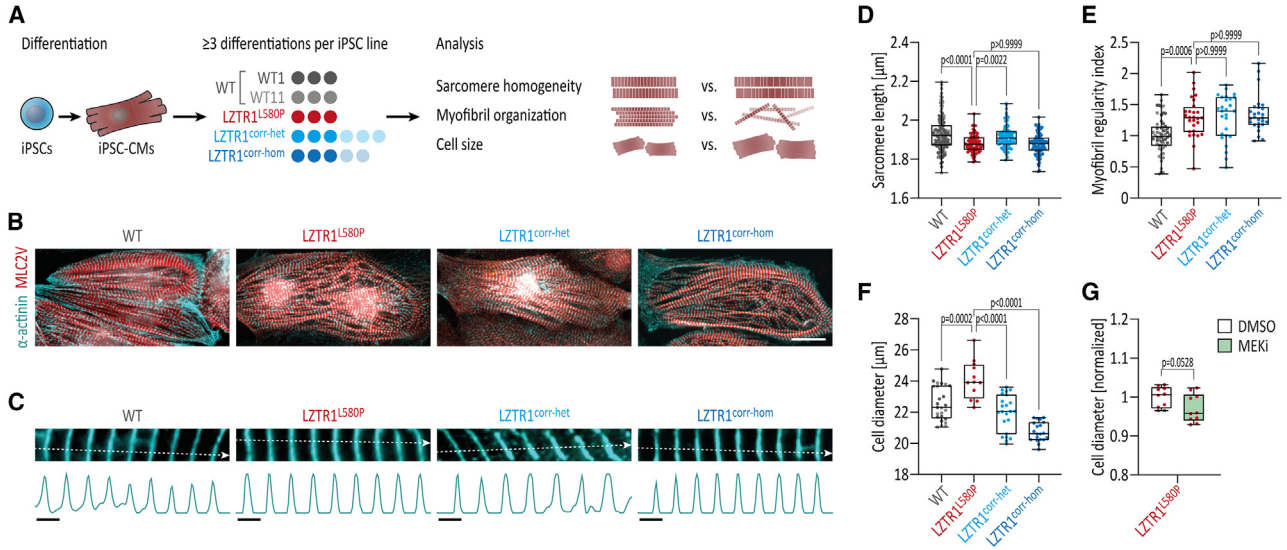

Figure 4. Homozygous *LZTR1*^{L580P} provokes cardiomyocyte hypertrophy

(A) Two WT, the patient-specific, and the 2 CRISPR-corrected iPSC lines were differentiated into ventricular iPSC-CMs and analyzed for sarcomere length, myofibril organization, and cell size at day 60 of differentiation.

(B) Representative images of iPSC-CMs stained for α-actinin and ventricular-specific MLC2V indicated a regular and well-organized sarcomeric assembly across all iPSC lines; scale bar: 20 μm.

(C) Analysis of the mean sarcomere length per cell was based on measurement of multiple α-actinin-stained individual myofibrils; representative myofibrils and corresponding intensity plots are shown; scale bar: 2 μm.

(D) Quantitative analysis displayed a typical sarcomere length in iPSC-CMs ranging from 1.7 to 2.2 μm across all iPSC lines; *n* = 75–135 cells from 3 individual differentiations per iPSC line.

(E) Quantitative analysis of the myofibril organization in iPSC-CMs, assessed by fast Fourier transform algorithm, demonstrated a high myofibril regularity across all iPSC lines; data were normalized to WT; *n* = 27–58 images from 3 individual differentiations per iPSC line.

(F) Quantitative analysis of the cell diameter in suspension in singularized iPSC-CMs, assessed by CASY cell counter, detected a hypertrophic cell diameter in the patient's cells, compared with WT and CRISPR-corrected iPSC-CMs; *n* = 12–25 samples from 3 to 6 individual differentiations per iPSC line.

(G) Quantitative analysis of the cell diameter in suspension in singularized patient-specific iPSC-CMs that were treated with MEKi trametinib or with DMSO for 5 days, assessed by CASY cell counter; *n* = 3 independent differentiations, with *n* = 3–4 individual wells per condition.

Data were analyzed by non-parametric Kruskal-Wallis test with Dunn correction (D–F) or unpaired t test (G) and are presented as mean ± SEM.

Since we did not observe increased ERK activity attributed to the homozygous *LZTR1*^{L580P} missense variant, we compared the patient-specific LZTR1^{L580P} cells with another patient line harboring biallelic truncating *LZTR1* variants (LZTR1^{KO}), which we reported in our previous study.[10] Here, higher levels of phosphorylated ERK were observed in the LZTR1^{KO} cultures under basal conditions and after stimulation (Figures 3F and 3G). Interestingly, LZTR1^{KO} iPSC-CMs exhibited a substantially higher accumulation of RAS GTPases compared to LZTR1^{L580P} cells, implying a partial residual function of LZTR1^{L580P} ubiquitin ligase complexes.

Homozygous LZTR1^{L580P} provokes cardiomyocyte hypertrophy

To elucidate the consequences of dysregulated RAS-MAPK signaling on the cellular characteristics of cardiomyocytes, we investigated sarcomere homogeneity, myofibril organization, and cell size of the patient-derived iPSC-CMs, the CRISPR-corrected cells, and WT controls at day 60 of differentiation (Figure 4A). All iPSC lines showed a well-organized sarcomeric organization with a pronounced striated expression of α-actinin and ventricular-specific MLC2V (Figure 4B). To analyze sarcomeric homogeneity, we measured the distances between the sarcomeric Z disks along individual myofibrils (Figure 4C). In agreement with the sarcomere length previously observed in neonatal and adult human hearts,[21] *LZTR1*-deficient as well as *LZTR1*-corrected and WT cells exhibited a typical sarcomere length ranging from 1.7 to 2.2 μm, with an average of approximately 1.9 μm across all iPSC lines (Figure 4D). As sarcomeric disarray has been frequently reported in other iPSC-CM models of both NS-associated and non-syndromic HCM,[15,22] we examined the myofibril organization in the individual iPSC-CMs. Quantitative analysis showed no decrease in sarcomere regularity or pathological myofibril organization in LZTR1^{L580P} cultures (Figure 4E). On the contrary, LZTR1^{L580P} and CRISPR-corrected iPSC-CMs even demonstrated a slightly higher myofibril regularity compared to unrelated controls, indicating that the pathological gene variant exerts no severe effect on sarcomere structures.

Since cardiomyocyte hypertrophy is a major hallmark of HCM, we further investigated the mean cell size of iPSC-CMs from all cell lines by utilizing our previously established assay to determine cell size in suspension.[10] Here, the patient's iPSC-CMs displayed a significant cellular enlargement compared to WT iPSC-CMs (Figure 4F). Strikingly, the hypertrophic phenotype was normalized in the CRISPR-corrected cells from both the

LZTR1$^{corr\text{-}het}$ and the LZTR1$^{corr\text{-}hom}$ isogenic cultures. Moreover, and in line with the molecular observations, heterozygous correction of the pathological variant was sufficient to significantly reduce cellular hypertrophy. Additionally, we assessed whether treatment with the MEK inhibitor trametinib for 5 days could reverse the cellular hypertrophy in the patient-specific iPSC-CMs (Figure 4G). No significant reduction in cell size was observed in MEKi-treated cells compared to DMSO-treated cells, suggesting that normalization of RAS-MAPK signaling activity is unable to alleviate the cellular pathology in the short term.

In summary, the patient's iPSC-CMs harboring the homozygous missense variant *LZTR1*^{L580P} recapitulated the cardiomyocyte hypertrophy *in vitro*. Importantly, CRISPR correction of the pathological variant was able to normalize the hypertrophic phenotype.

Homozygous LZTR1^{L580P} does not compromise contractile function

NS-associated and non-syndromic HCM are frequently associated with contractile dysfunction, and these patients are at risk of developing arrhythmias.[23,24] We generated engineered heart muscles (EHMs) from diseased, CRISPR-corrected, and WT iPSC-CMs enabling us to investigate the functional characteristics in a three-dimensional environment more closely resembling the native conditions of the human heart muscle (Figure S4A).[25,26] Microscopically, all iPSC lines formed homogeneous cardiac tissues without showing apparent cell line-dependent differences after 6 weeks of maturation (Figure S4B). Optical measurements were performed to study beating rate, force of contraction, and contraction kinetics in spontaneously contracting EHMs (Figures S4C–S4H). In comparison to WT EHMs, an increased spontaneous beat frequency was detected in the LZTR1^{L580P} EHMs. The beat rate acceleration was gradually normalized in the heterozygous and homozygous corrected variants. Low beat-to-beat variability indicated that the LZTR1 mutant tissues do not provoke arrhythmia. No significant differences in force of contraction were identified. In accordance with higher beat frequencies, an acceleration of contraction and relaxation kinetics were observed in LZTR1^{L580P}-, LZTR1$^{corr\text{-}het}$-, and the LZTR1$^{corr\text{-}hom}$-derived EHMs. However, since the altered kinetics were noticed in both diseased and CRISPR-corrected tissues, this rather suggested a mutation-independent effect. In addition, we examined the contractile properties of monolayer cultures by video analysis and did not observe any significant differences between WT, patient-specific, CRISPR-corrected, and LZTR1^{KO} iPSC-CMs (Figure S5).

Taken together, these functional data indicate that the missense variant *LZTR1*^{L580P} does not impact the contractile function and rhythmogenesis of cardiomyocytes.

Homozygous LZTR1^{L580P} induces polymerization of LZTR1 proteins

Considering the severe consequence of *LZTR1*^{L580P} on the molecular and cellular pathophysiology in cardiomyocytes, we aimed to determine the specific effect of this variant on protein structure, complex formation, as well as its subcellular localization. We were unable to visualize endogenous LZTR1 in our cell model by immunocytochemistry, by testing several commercial antibodies, or by N-terminal or C-terminal genetic tagging of the *LZTR1* gene locus. To circumvent these obstacles, we established ectopic expression of tagged *LZTR1* in WT iPSC-CMs at around day 60 of differentiation by lipofectamine-based plasmid transfection (Figure 5A). Besides *LZTR1*^{WT} and *LZTR1*^{L580P}, we screened the NS patient database (NSeuroNet)[27] for additional missense variants classified as likely pathogenic or variant of uncertain significance and located in close proximity to *LZTR1*^{L580P} (within the BACK1 domain), and included them in our screening panel (Figure 5B). Of note, except for *LZTR1*^{L580P} and *LZTR1*^{E563Q},[7] none of the other variants had been reported to be present in homozygosity in *LZTR1*-associated NS. In addition, we included a truncating variant *LZTR1*$^{\Delta BTB2\text{-}BACK2}$, which lacks the entire BTB2-BACK2 domain and mimics the genotype of the two siblings described in our previous study.[10]

As previously observed in other cell types (e.g., HeLa,[8] HEK293[28]), LZTR1^{WT} appeared as a dotted pattern evenly distributed throughout the cell (Figures 5C and S6A). A similar dotted appearance was observed for the variants LZTR1^{E563Q}, LZTR1^{I570T}, LZTR1^{V579M}, LZTR1^{E584K}, and LZTR1^{R619H}. As expected, the truncating variant LZTR1$^{\Delta BTB2\text{-}BACK2}$ showed a mislocalized homogeneous cytoplasmic distribution. Surprisingly, LZTR1^{L580P} formed large filaments in the cytoplasm (Figures 5C and S6A). To verify this initial finding, we co-expressed two differentially tagged *LZTR1* constructs and evaluated their overlap within the cells. Consistently, LZTR1^{L580P} appeared as large protein polymers, whereas LZTR1^{WT} remained speckle-like (Figure 5D). As *LZTR1*^{L580P} in the heterozygous state did not induce a disease phenotype based on clinical and experimental evidence, we hypothesized that the co-expression of LZTR1^{L580P} and LZTR1^{WT} might resolve the polymer chains. Strikingly, the LZTR1^{L580P}-induced filaments dispersed when co-expressed with the WT variant, implicating that the LZTR1 complexes exclusively assemble into protein polymers when the specific *LZTR1*^{L580P} missense variant is present on both alleles (Figure 5E). To quantitatively analyze these observations, we established an automated image-based speckle/filament recognition and computation (Figure S6B). While LZTR1^{WT} displayed a mean speckle size of 0.9 μm, the mean filament length per cell in LZTR1^{L580P} amounted to 7.9 μm (Figure 5F). Co-expression of mutant and WT constructs, and vice versa, normalized the speckle size to 1.2 μm and 1.3 μm, respectively.

These data provide evidence that the missense variant *LZTR1*^{L580P} induces polymerization of LZTR1 proteins, which may subsequently compromise the proper function of the ubiquitination machinery.

Homozygous LZTR1^{L580P} alters binding affinities of dimerization domains

Proteins from the BTB-BACK-Kelch domain family, including LZTR1, are predicted to assemble into homo-dimers.[9,28,29] However, our current knowledge regarding the exact domains responsible for LZTR1 dimerization is limited. To identify a plausible explanation for the *LZTR1*^{L580P}-induced polymerization, we utilized ColabFold, an AlphaFold-based platform for predicting protein structures and homo- and heteromer complexes.[30] We used a homo-trimer configuration of the experimentally

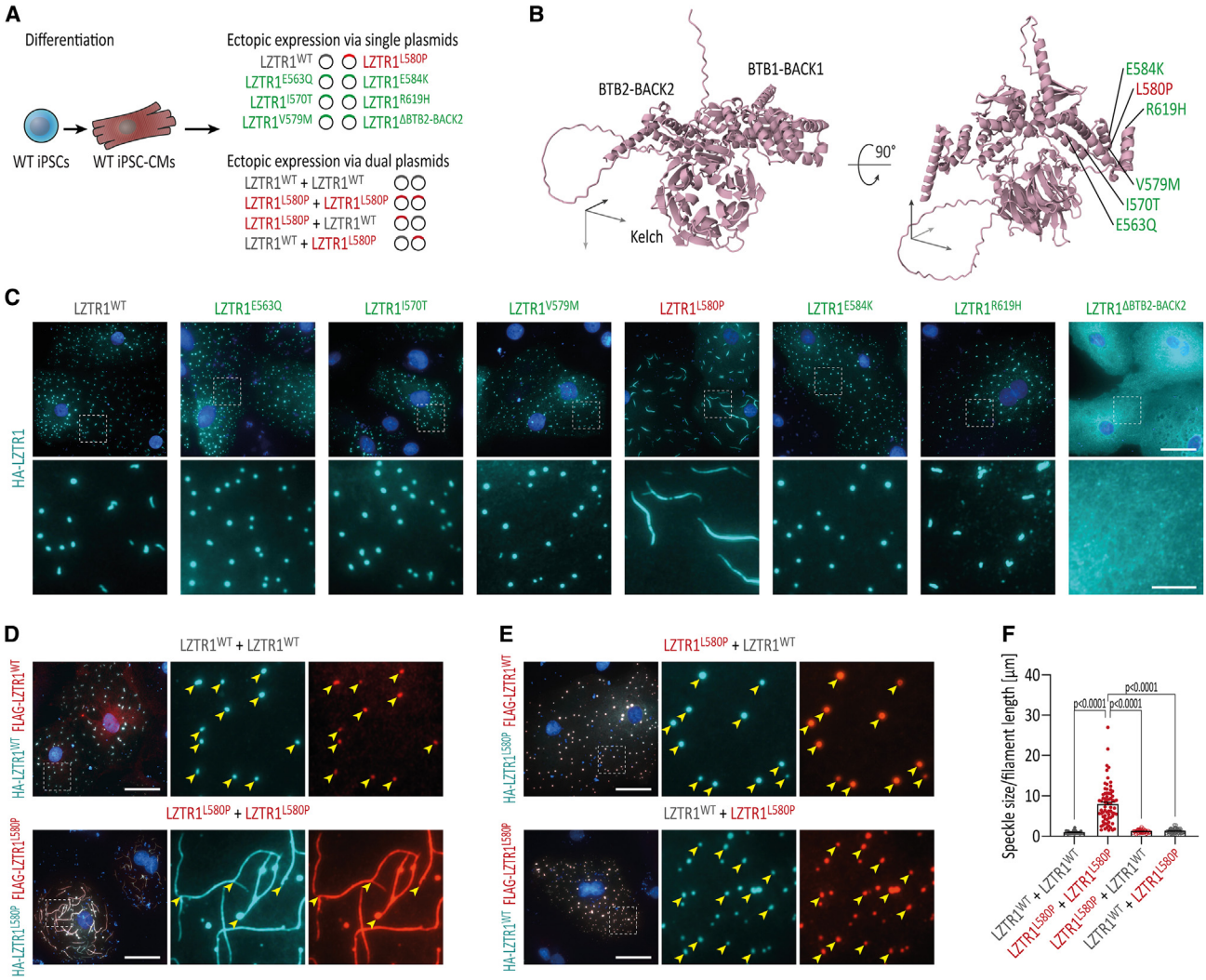

Figure 5. Homozygous *LZTR1*^{L580P} induces polymerization of LZTR1 proteins

(A) WT iPSCs were differentiated into ventricular iPSC-CMs, transfected at day 60 of differentiation with plasmids for ectopic expression of LZTR1 variants, and analyzed 24 h post-transfection for subcellular localization LZTR1 complexes.

(B) AlphaFold protein structure of monomeric LZTR1 highlighting the location of selected variants within the BACK1 domain.

(C) Representative images of iPSC-CMs after single plasmid transfection stained for hemagglutinin (HA)-tagged LZTR1 showed that LZTR1^{WT} and most other variants present a speckle-like pattern equally distributed throughout the cytoplasm, whereas missense variant LZTR1^{L580P} forms large filaments; nuclei were counter-stained with Hoechst 33342 (blue); scale bars: 20 µm (top), 5 µm (bottom).

(D and E) Representative images of iPSC-CMs after dual plasmid transfection stained for HA-tagged and FLAG-tagged LZTR1 confirmed the filament formation of LZTR1^{L580P} (D), whereas co-expression of LZTR1^{WT} and LZTR1^{L580P} in different combinations resolved the polymer chains (E); nuclei were counter-stained with Hoechst 33342 (blue); scale bar: 20 µm.

(F) Quantitative analysis of the mean speckle size and mean filament length per cell of HA-tagged LZTR1 in co-transfected iPSC-CMs, assessed by a customized CellProfiler pipeline, confirmed the formation of *LZTR1*^{L580P}-induced filaments; *n* = 34–74 cells per condition. Data were analyzed by non-parametric Kruskal-Wallis test with Dunn correction and are presented as mean ± SEM (F).

employed *LZTR1* variants (all within the BACK1 domain), and the AlphaFold-multimer predicted five high-quality models, each with an average predicted local distance difference test (a per-residue confidence metric) between 64.1 and 76.0. For all variants, we inspected the interaction between the chains through the predicted alignment error (PAE) generated by AlphaFold-multimer (Figure S7). A low PAE indicates that interfacing residues were correctly predicted across chains. Based on these predictions, we compared the top-ranked models of each variant according to the predicted template modeling score, which corresponded to overall topological accuracy (Figure 6A). The top-ranked model for LZTR1^{WT} showed interaction as a homo-dimer via the BACK2-BACK2 domain, while the third LZTR1 protein remained monomeric. We also observed the identical dimerization via the BACK2 domains for all other variants, except for LZTR1^{L580P} (Figure S7). In contrast, the top-ranked

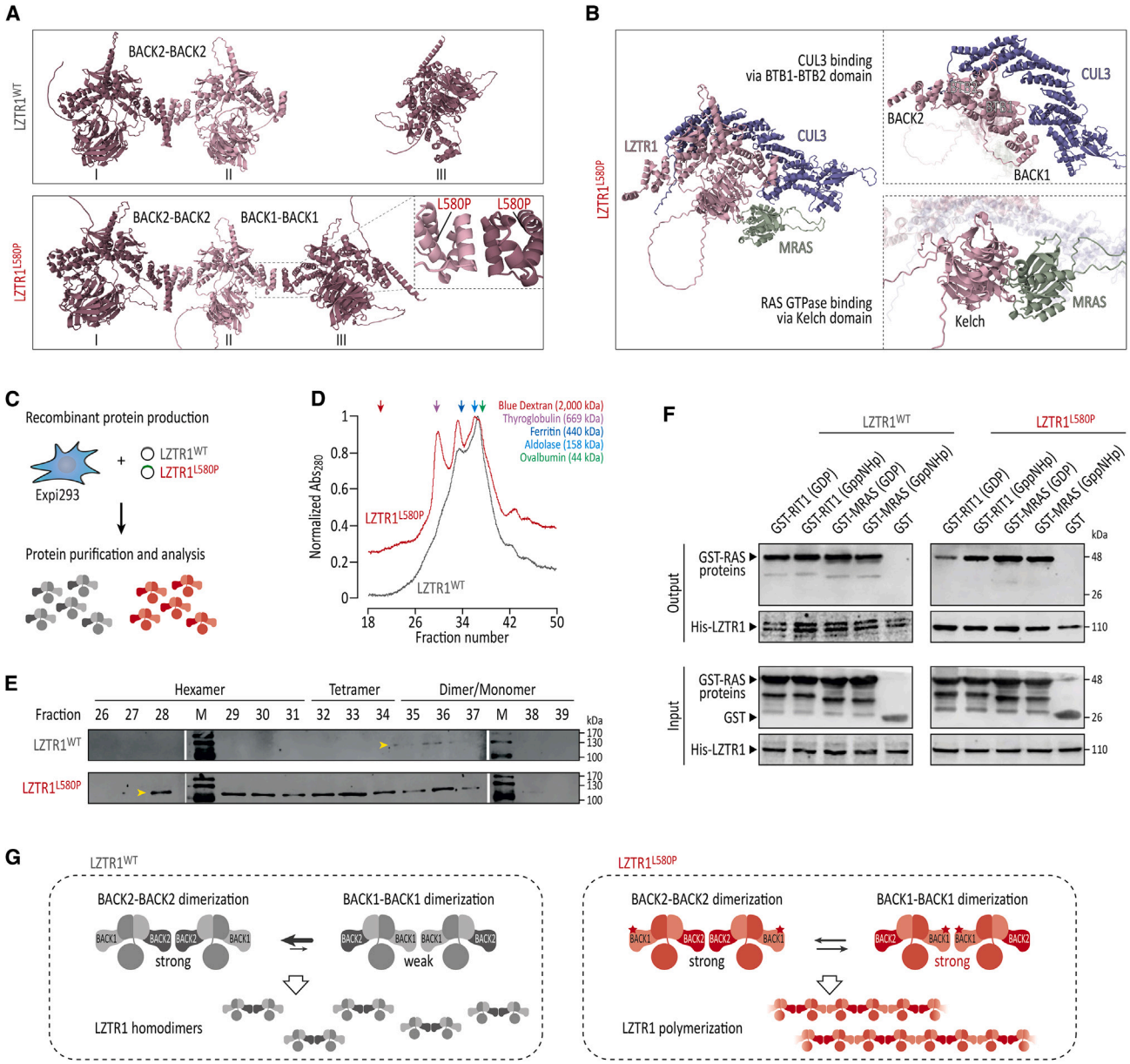

Figure 6. Homozygous *LZTR1*^{L580P} alters binding affinities of dimerization domains

(A) Computational modeling of the top-ranked LZTR1 homo-trimer interactions by ColabFold predicted a dimer plus monomer configuration via BACK2-BACK2 dimerization for LZTR1^{WT}, whereas LZTR1^{L580P} was predicted to form linear trimers via BACK2-BACK2 and BACK1-BACK1 dimerization.

(B) Computational modeling of the interaction between LZTR1^{L580P} and its binding partners predicted binding to cullin 3 (CUL3) via the BTB1-BTB2 domain and to MRAS via the Kelch domain.

(C) Production of LZTR1^{WT} and LZTR1^{L580P} recombinant proteins from Expi-293F cells for characterization of molecular masses of proteins and protein complexes.

(D) Analytical size-exclusion chromatography of soluble recombinant LZTR1 proteins detected a higher-order oligomerization profile for LZTR1^{L580P} compared to the less complex elution profile of LZTR1^{WT}.

(E) Immunoblotting of the fractions showed elution of LZTR1^{L580P} as hexamer, tetramer, and dimer/monomer, whereas LZTR1^{WT} eluted predominantly as dimer/monomer.

(F) Pull-down assay analysis showed comparable binding affinities of LZTR1^{WT} and LZTR1^{L580P} with MRAS and RIT1 proteins in both inactive (GDP-bound) and active (GppNHp-bound) states.

(G) Model for LZTR1 complex formation: whereas LZTR1^{WT} assembles in homo-dimers via the BACK2-BACK2 dimerization domain, LZTR1^{L580P} may alter the binding affinity of the BACK1 domain, causing the formation of linear LZTR1 polymer chains via dimerization of both BACK2 and BACK1 domains.

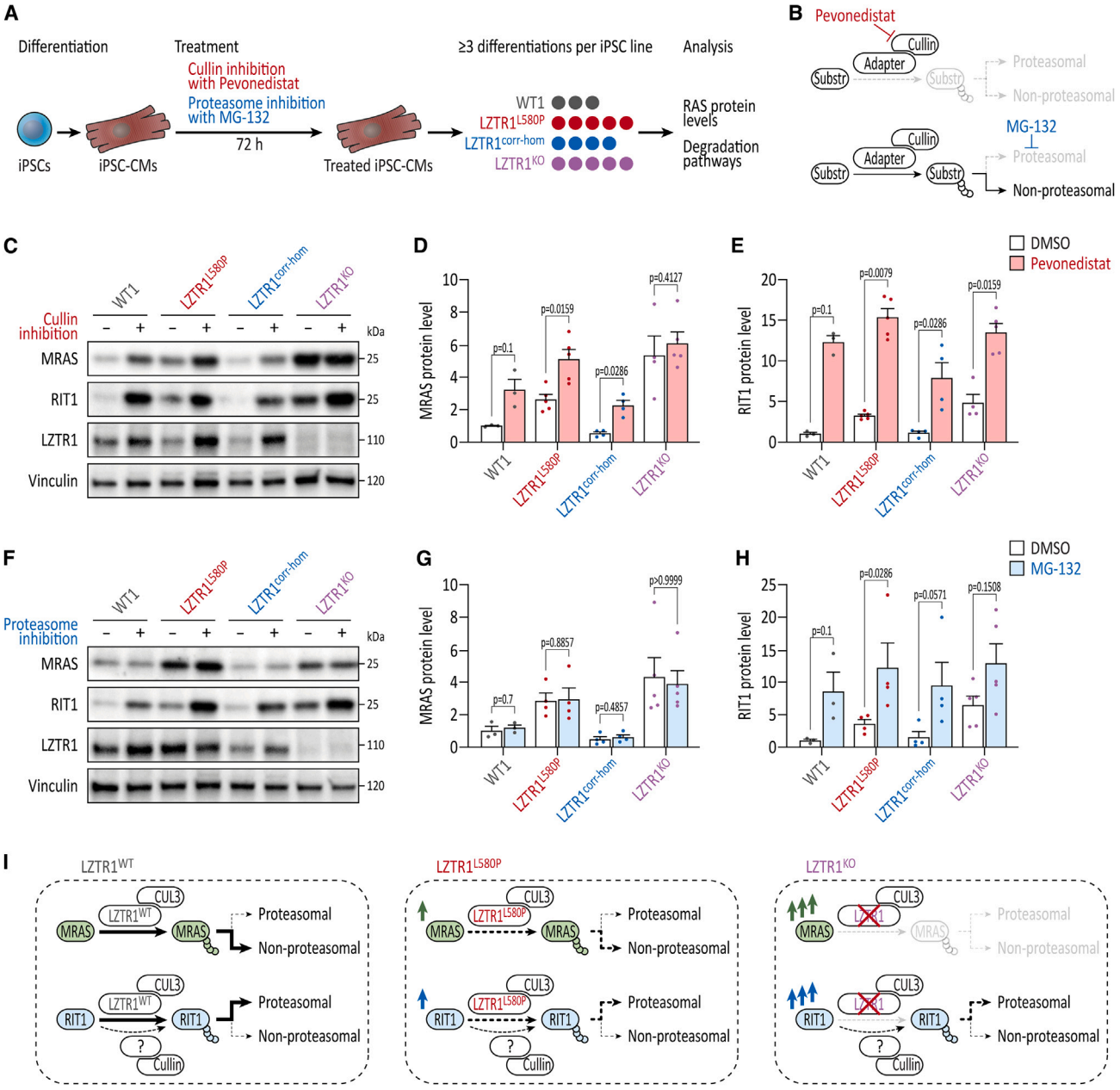

Figure 7. Homozygous *LZTR1*^{L580P} retains residual protein

(A) WT, the patient-specific, the homozygous CRISPR-corrected, and LZTR1^{KO} iPSC lines were differentiated into ventricular iPSC-CMs and treated with pevonedistat and MG-132 for 3 days to analyze the ubiquitin-mediated degradation of RAS GTPases; *n* = 3–5 individual differentiations/treatments per iPSC line.

(B) Mode of action of pevonedistat and MG-132 on degradation pathways: pevonedistat is a selective NEDD8-activating enzyme inhibitor, preventing neddylation of cullin RING ligases and blocking ubiquitin-mediated degradation via the proteasome and other degradation pathways, whereas MG-132 is a selective inhibitor specifically blocking the proteolytic activity of the 26S proteasome.

(C) Representative blots showing MRAS, RIT1, and LZTR1 levels in iPSC-CMs upon pevonedistat treatment for 3 days, assessed by western blot; vinculin served as loading control.

(D and E) Quantitative analysis of western blots for MRAS (D) and RIT1 (E) upon pevonedistat treatment; data were normalized to total protein and to the DMSO-treated WT samples on each membrane.

(F) Representative blots showing MRAS, RIT1, and LZTR1 levels in iPSC-CMs upon MG-132 treatment for 3 days, assessed by western blot; vinculin served as loading control.

(G and H) Quantitative analysis of western blots for MRAS (G) and RIT1 (H) upon MG-132 treatment; data were normalized to total protein and to the DMSO-treated WT samples on each membrane.

(legend continued on next page)

model for LZTR1^{L580P} predicted an interaction between all three chains, on the one hand via the BACK2-BACK2 domain and on the other hand via the BACK1-BACK1 domain (Figure 6A). In addition, we used AlphaFold-multimer to predict the interaction of LZTR1^{L580P} with the substrate MRAS and the ubiquitin ligase cullin 3 (Figure 6B). Within the multiprotein complex, MRAS was predicted to bind to the Kelch domain, whereas cullin 3 was predicted to interact with the BTB1-BTB2 domain of LZTR1.

To experimentally confirm the formation of LZTR1^{L580P} polymers, we produced soluble recombinant proteins of LZTR1^{WT} and LZTR1^{L580P} and analyzed the purified samples by analytical size-exclusion chromatography, allowing us to characterize the molecular masses of protein complexes (Figure 6C). A higher-order oligomerization profile was observed for LZTR1^{L580P}, whereas LZTR1^{WT} exhibited a less complex elution profile (Figure 6D). Immunoblotting of the fractions showed that LZTR1^{L580P} eluted as a hexamer with a molecular weight of approximately 700 kDa, as a tetramer corresponding to 450–550 kDa, and as a dimer/monomer with a molecular weight of 100–200 kDa (Figure 6E). In contrast, LZTR1^{WT} was characterized by a single peak, indicative of its predominantly dimeric/monomeric state. In addition, we examined the interaction of LZTR1^{WT} and LZTR1^{L580P} proteins with RIT1 and MRAS in their inactive (guanosine diphosphate [GDP]-bound) and active (GppNHp-bound; GppNHp is a non-hydrolyzable GTP analog) states. Both LZTR1^{WT} and mutant LZTR1^{L580P} were capable of binding their substrates in both nucleotide-bound states (Figure 6F).

Collectively, the *in silico* predictions and molecular analyses suggest that the missense variant *LZTR1^{L580P}* alters the binding affinities of the BACK1 domain, enabling the formation of linear LZTR1 polymer chains via both dimerization domains, thereby providing a rationale for the molecular and cellular impairments in NS (Figure 6G).

Homozygous LZTR1^{L580P} retains residual protein function

To investigate how severely the degradation of RAS GTPases is affected by the missense variant LZTR1^{L580P} (especially compared to the complete loss of LZTR1), we treated the patient-specific iPSC-CMs, the CRISPR-corrected cells, the LZTR1^{KO} cells, and the WT controls with the cullin RING ligase inhibitor pevonedistat (which blocks the ubiquitin-mediated degradation via the proteasome and other degradation pathways) or the proteasome inhibitor MG-132 and analyzed MRAS and RIT1 protein levels 3 days after treatment (Figures 7A and 7B). As expected, the inhibition of cullin-mediated ubiquitination by pevonedistat increased MRAS and RIT1 protein levels in WT and CRISPR-corrected iPSC-CMs (Figures 7C–7E). Treatment in patient-specific LZTR1^{L580P} cultures further increased the RAS GTPase levels, indicating residual function of the LZTR1^{L580P}-cullin 3 ubiquitin ligase complex. Interestingly, while MRAS accumulation in LZTR1^{KO} cultures could not be further increased by cullin inhibition, RIT1 protein levels were significantly higher after treatment in *LZTR1*-deficient cells. This suggests that MRAS is exclusively targeted for degradation by the LZTR1-cullin 3 ubiquitin ligase complex, whereas RIT1 can be additionally degraded in an *LZTR1*-independent manner. Furthermore, inhibition of the ubiquitin-proteasome system resulted in increased RIT1 levels, suggesting that RIT1 is predominantly degraded by the proteasomal pathway (Figures 7F–7H). In contrast, MRAS levels were not affected after treatment across all iPSC lines, indicating the degradation of MRAS by predominantly non-proteasomal pathways.

These data confirm that the missense variant *LZTR1^{L580P}* preserves some residual function compared to the complete loss of *LZTR1*. Furthermore, the results demonstrate that degradation of cardiomyocyte-specific MRAS is exclusively mediated by LZTR1 via non-proteasomal pathways, whereas degradation of RIT1 is mediated by both *LZTR1*-dependent and *LZTR1*-independent pathways.

DISCUSSION

Both autosomal dominant and autosomal recessive forms of *LZTR1*-associated NS have been described presenting with a broad clinical spectrum and various phenotypic expressions of symptoms. However, the mechanistic consequences of many of these mutations, mostly classified as variants of uncertain significance, are still under debate. In previous studies, we and others elucidated the role of LZTR1 as a critical negative regulator of the RAS-MAPK pathway by controlling the pool of RAS GTPases.[8–10,28,31] Using patient-derived iPSC-CMs from NS patients with biallelic truncating *LZTR1* variants, we have shown that *LZTR1* deficiency results in the accumulation of RAS levels, signaling hyperactivity and cardiomyocyte hypertrophy.[10] Furthermore, by genetically correcting one of the two affected alleles, we could show that one functional *LZTR1* allele is sufficient to maintain normal RAS-MAPK activity in cardiac cells. In contrast to the truncating variants, dominant *LZTR1* missense variants generally cluster in the Kelch motif. Based on heterologous expression systems, these dominant variants are considered to interfere with the recognition or binding of RAS substrates to the LZTR1 ubiquitination complex.[8,9,11,31] Much less is known about the functional relevance of recessive *LZTR1* missense variants, which are distributed throughout the entire protein. Detailed insights into specific structure-function relationships of LZTR1 are crucial to facilitate the development of patient-specific therapies.

In this study, we diagnosed a patient who presented with typical clinical features of NS, including an early-onset HCM, and confirmed this diagnosis on a genetic level by identifying the homozygous variant c.1739T>C/p.L580P in *LZTR1*. The variant has not been previously described in patients with NS,

(I) Model for LZTR1-mediated degradation of MRAS and RIT1 for LZTR1^{WT}, LZTR1^{L580P}, and LZTR1^{KO}: (left) MRAS is exclusively targeted by the LZTR1^{WT}-cullin 3 ubiquitin ligase complex for degradation, whereas RIT1 is additionally ubiquitinated by other cullin ubiquitin ligases and degraded predominantly by the proteasome; (center) the LZTR1^{L580P} decreases degradation of MRAS and RIT1; and (right) loss of LZTR1 completely prevents MRAS degradation, while RIT1 degradation remains functional to some extent in an LZTR1-independent manner.
Data were analyzed by non-parametric Kruskal-Wallis test with Dunn correction and are presented as mean ± SEM (D, E, G, and H).

and we classified *LZTR1*^{L580P} as likely causative based on its absence in gnomAD and our computational prediction. Apart from the *LZTR1* variant, no additional variants were detected in other NS-associated genes or RAS-associated candidates. By combining *in vitro* disease modeling using patient-specific and CRISPR-Cas9-corrected iPSC-CMs with molecular and cellular phenotyping and *in silico* structural modeling, we identified a *LZTR1*^{L580P}-specific disease mechanism provoking the cardiac pathology of NS. In detail, we found that (1) *LZTR1*^{L580P} is predicted to alter the binding affinity of the BACK1 dimerization domain that facilitates the formation of linear LZTR1 protein chains; (2) homozygous *LZTR1*^{L580P} fosters the assembly of large polymers of LZTR1 proteins causing LZTR1 complex dysfunction; (3) pathological LZTR1 complexes result in impaired degradation and accumulation of RAS GTPases and RAS-MAPK signaling hyperactivity; and (4) increased signaling activity induces global changes in the proteomic landscape, ultimately causing cellular hypertrophy. Importantly, correction of one allele—in line with the co-expression of WT and mutant *LZTR1* transcripts—is sufficient to normalize the cardiac disease phenotype at both molecular and cellular levels.

Based on recent publications, there is a broad consensus on the role of LZTR1 as an adaptor protein for the cullin 3 ubiquitin ligase complex targeting RAS proteins for ubiquitination and subsequent degradation.[8–11,28,31] In line with observations in other NS-associated genes and mutations, LZTR1 dysfunction and concomitant accumulation of RAS GTPases result in the hyperactivation of RAS-MAPK signaling. We confirmed robustly elevated RAS levels in patient-specific cells harboring the homozygous *LZTR1*^{L580P} missense variant. However, the accumulation of RAS GTPases and ERK hyperactivity was substantially higher in LZTR1^{KO} cells, supporting a partial residual function of LZTR1^{L580P} ubiquitin ligase complexes. Furthermore, it remains controversial whether LZTR1 is able to recognize all members of the RAS GTPase family for degradation or whether there is a selective affinity toward particular RAS members. Using heterologous expression systems, LZTR1 has been shown to interact with the highly conserved RAS proteins HRAS, KRAS, and NRAS.[8,28,31] However, Castel and colleagues observed a selective binding of LZTR1 to RIT1 and MRAS, but not to HRAS, KRAS, or NRAS.[9] Moreover, in homozygous *LZTR1* knockout mice, elevated RIT1 protein levels were detected in different organs, including brain, liver, and heart, while HRAS, KRAS, and NRAS levels remained unchanged.[32] Using global proteomics, we now provide further evidence that LZTR1 dysfunction in cardiomyocytes causes severe accumulation of MRAS and RIT1 and, to a lesser extent, elevation of the other RAS GTPases HRAS, KRAS, and NRAS, although all RAS proteins are robustly expressed in this cell type. We conclude that based on gene expression data and total protein levels, MRAS appears to be the most prominent RAS candidate in cardiomyocytes, driving the signaling hyperactivity in these cells. In addition, our inhibition experiments demonstrate that MRAS degradation is exclusively mediated by LZTR1 via proteasome-independent mechanisms, whereas RIT1 degradation is mediated by both LZTR1-dependent and LZTR1-independent pathways. These observations suggest that at endogenous expression levels, LZTR1 has a certain selectivity for MRAS and RIT1 and a lower affinity for the RAS GTPases HRAS, KRAS, and NRAS. However, we cannot exclude the possibility of cell-type-specific differences in LZTR1-RAS binding affinities.

Major hallmarks of pathological cardiac hypertrophy include impaired cardiac function, changes in extracellular matrix composition, fibrosis, and metabolic reprogramming and mitochondrial dysfunction.[33] In accordance, the proteomic disease signature of patient-derived iPSC-CM cultures detected impairments in muscle contraction, extracellular matrix organization, and metabolism—all crucial for proper cardiomyocyte function. Furthermore, *LZTR1*^{L580P}-derived iPSC-CMs recapitulated the patient's hypertrophic phenotype reflected by cellular enlargement. Strikingly, both the molecular profile and cellular hypertrophy were resolved upon CRISPR correction of the missense variant. Interestingly, no myofibrillar disarray was observed in our cell model. However, the presence of myofibril disarray in NS remains controversial: whereas structural defects were described in *RAF1*-associated iPSC models,[15,34] we and others did not observe any impact on sarcomere structures or myofibril organization in *LZTR1*-related, *PTPN11*-related, and *BRAF*-related iPSC-CMs,[10,14,16] implying potential genotype-dependent differences in the manifestation of myofibril disassembly in NS.

Missense variants in *LZTR1* located within the Kelch domain are predicted to affect substrate recognition, whereas missense variants in the BTB-BACK domain are assumed to impair either cullin 3 binding, proper homo-dimerization, or correct subcellular localization. Several studies have demonstrated that dominantly acting Kelch domain variants disrupt the recognition of RAS substrates but do not affect LZTR1 complex stability or subcellular localization.[8,9,11,31,35] In contrast, BTB-BACK missense variants showed no influence on RIT1 binding.[9,35] However, variants located in the BTB1 or the BTB2 domain, such as *LZTR1*^{V456G}, *LZTR1*^{R466Q}, *LZTR1*^{P520L}, and *LZTR1*^{R688C}, caused a subcellular mislocalization from defined speckles to a diffuse cytoplasmic distribution, similar to the findings obtained with truncating *LZTR1* variants.[8,31] In addition to these distinct pathological consequences of different variants analyzed so far, we now provide evidence for an alternative disease mechanism specific to the BACK1 domain-located *LZTR1*^{L580P}; ectopic expression of *LZTR1*^{L580P} in iPSC-CMs caused a pathological polymerization of LZTR1 ubiquitination complexes. This phenomenon was verified by *in silico* prediction and chromatography with purified recombinant LZTR1 proteins. In contrast, the binding probabilities of *LZTR1*^{L580P} to substrates and interaction partners were not significantly affected by the mutation. This remarkable phenotype was not observed for any other variant within the BACK1 domain. Notably, ectopic co-expression of *LZTR1*^{L580P} and *LZTR1*^{WT} alleviated polymerization, indicating that the assembly of LZTR1 polymer chains exclusively occurs when mutated proteins are present in the homozygous state. Oligomerization of another BTB-BACK family member had been reported previously: Marzahn and colleagues described that dimers from the cullin 3 ubiquitin ligase substrate adaptor SPOP (harboring only one BTB-BACK domain) self-associate into linear higher-order oligomers via BACK domain dimerization.[36] These SPOP oligomers assembled in membraneless cellular bodies, visualized as nuclear speckles, and it was proposed that the speckles may be important hotspots of ubiquitination. Based on these findings and our

data, we propose that LZTR1 complexes concentrate in cellular speckles (either as dimers or as oligomers) to form subcellular clusters for efficient ubiquitination and degradation of RAS proteins. However, *LZTR1*^{L580P}-induced polymerization of these complexes disrupts their proper function, leading to the accumulation of substrates. CRISPR-based correction was able to rescue the polymerization phenotype and may be a sustainable treatment option in the future. Alternatively, it may be possible to identify compounds that specifically prevent the interaction of LZTR1 complexes via BACK1-BACK1 dimerization.

Our knowledge of the specific domains responsible for LZTR1 homo-dimerization is still incomplete. While Castel and colleagues proposed that the BTB1 and the BACK1 domains are required for dimerization,[9] Steklov et al. observed impaired assembly in a BACK2 domain mutant *LZTR1* variant.[31] Based on *in silico* modeling, we now propose that LZTR1 can dimerize via either the BACK2-BACK2 domains or the BACK1-BACK1 domains. Although BACK2-BACK2 dimerization may be primarily utilized in LZTR1^{WT}, changes in the binding affinities of the BACK1 domain as a consequence of *LZTR1*^{L580P} facilitated tandem self-association of dimers to linear multimers.

Limitations of the study

So far, the relevance of certain *LZTR1* missense variants have been investigated in heterologous expression systems, failing to faithfully represent human cardiac physiology. Our study demonstrates the potential of patient-specific iPSCs to model human diseases and to detect variant-specific pathomechanisms. Despite the great advantages of this model system over other cellular models, iPSC-CMs possess certain limitations. As summarized by several reports, iPSC-CMs are considered to be developmentally immature characterized by molecular and functional properties similar to fetal CMs.[25,37,38] Although we complemented our study by utilizing three-dimensional EHMs, these *in vitro* models are currently not able to entirely resemble the disease phenotype at the organ level. EHM data showed altered kinetics between CRISPR-corrected and WT cells. Although these differences are likely consequences of different genetic backgrounds and potential disease-modifier variants, a manifested impairment in the patient fibroblasts (e.g., due to LZTR1 dysfunction) that persists after reprogramming and cardiac differentiation cannot be excluded. Due to unsuccessful genetic tagging of LZTR1 in iPSCs, the mutation-induced polymerization phenotype could only be observed by overexpression, which does not entirely reflect the endogenous condition. Furthermore, although different concentrations and time points were evaluated in iPSC-CMs prior to the inhibitor experiments, these experiments can only capture a snapshot of the degradation machinery, and additional experiments may be necessary to fully dissect the degradation pathway of RAS proteins. Although the *in silico* modeling by AlphaFold was consistent with the experimental data, this analysis must be undertaken with caution because the AlphaFold-multimer was not trained with single point variants in mind. In addition, due to technical prerequisites, we were unable to predict whether the trend would remain consistent for complexes with more than three chains.

Taken together, this study identified a specific mechanism causing recessive NS, which is initiated by *LZTR1*^{L580P}-induced polymerization of LZTR1 complexes, provoking molecular and cellular impairments associated with cardiac hypertrophy. Moreover, CRISPR correction of the missense variant on one allele was sufficient to rescue the phenotype, thereby providing proof of concept for a sustainable therapeutic approach.

STAR★METHODS

Detailed methods are provided in the online version of this paper and include the following:

- KEY RESOURCES TABLE
- RESOURCE AVAILABILITY
  - Lead contact
  - Materials availability
  - Data and code availability
- EXPERIMENTAL MODEL AND STUDY PARTICIPANT DETAILS
  - Human iPSC lines
  - Ethical approval
- METHOD DETAILS
  - Whole exome sequencing
  - Generation and culture of human iPSCs
  - Cardiomyocyte differentiation of iPSCs and generation of engineered heart muscle
  - Biosensor-based analysis of ERK signaling dynamics in iPSC-CMs
  - Proteomics and Western blot analysis of iPSC-CMs
  - Real-time PCR analysis of iPSC-CMs
  - Analysis of sarcomere length and myofibril organization of iPSC-CMs
  - Analysis of cell size of iPSC-CMs
  - Video-based contractility analysis of iPSC-CMs
  - Ectopic expression of LZTR1 variants in iPSC-CMs
  - Expression and purification of recombinant LZTR1 proteins
  - Analytical size exclusion chromatography (SEC) of soluble recombinant LZTR1 proteins
  - Pull-down assay for analysis of LZTR1-RAS interactions
  - In silico prediction of protein structures and multimer complexes
- QUANTIFICATION AND STATISTICAL ANALYSIS

SUPPLEMENTAL INFORMATION

Supplemental information can be found online at https://doi.org/10.1016/j.celrep.2024.114448.

ACKNOWLEDGMENTS

We thank Laura Cyganek, Yvonne Hintz, Nadine Gotzmann, Lisa Schreiber, and Yvonne Wedekind (Stem Cell Unit, University Medical Center Göttingen), Branimir Berečić, Tim Meyer, and Malte Tiburcy (Institute of Pharmacology and Toxicology, University Medical Center Göttingen), and Anja Wiechert and Manuela Gesell Salazar (Interfaculty Institute of Genetics and Functional Genomics, University Medicine Greifswald) for excellent technical assistance. This work was supported by the German Research Foundation (DFG) project nos. 417880571 and 501985000 to L.C., project no. 408077919 to I.C.C., project no. 193793266, Collaborative Research Center 1002, C04, D01, D02, and S01 to W.-H.Z., G.H., B.W., and L.C., and project no. 390729940, Germany's Excellence Strategy - EXC 2067/1 to A.V.B., G.H., W.-H.Z., B.W., and L.C.; the Else Kroner-Fresenius Foundation project no. 2019_A75 to L.C.; the German Federal Ministry of Education and Research (BMBF)/DZHK to E.H., G.H., W.-H.Z., B.W., and L.C.; the BMBF GeNeRARe project nos. 01GM1902F and 01GM1519D to I.C.C. and M.R.A.; and the Leducq Foundation project no. 20CVD04 to W.-H.Z.

AUTHOR CONTRIBUTIONS

Conceptualization, L.C. Investigation, A.V.B., O.G.-G., E.H., F.K., A.M., M.S., L.B., M.K., M.E., J.A., F.M., and L.C. Methodology, A.V.B., O.G.-G., and

L.C. Software, C.P. and H.S. Resources, I.C.C., L.G., D.W., and W.-H.Z. Supervision, G.H., W.-H.Z., M.R.A., and B.W. Visualization, L.C. Writing – original draft, L.C. Writing – review & editing, L.C., A.V.B., and O.G.-G. Funding acquisition, E.H., I.C.C., G.H., W.-H.Z., M.R.A., B.W., and L.C.

DECLARATION OF INTERESTS

The authors declare no competing interests.

Received: January 13, 2024
Revised: April 3, 2024
Accepted: June 20, 2024
Published: July 13, 2024

REFERENCES

1. Roberts, A.E., Allanson, J.E., Tartaglia, M., and Gelb, B.D. (2013). Noonan syndrome. Lancet *381*, 333–342. https://doi.org/10.1016/S0140-6736(12)61023-X.
2. Linglart, L., and Gelb, B.D. (2020). Congenital heart defects in Noonan syndrome: Diagnosis, management, and treatment. Am. J. Med. Genet. C Semin. Med. Genet. *184*, 73–80. https://doi.org/10.1002/ajmg.c.31765.
3. Hickey, E.J., Mehta, R., Elmi, M., Asoh, K., McCrindle, B.W., Williams, W.G., Manlhiot, C., and Benson, L. (2011). Survival implications: hypertrophic cardiomyopathy in Noonan syndrome. Congenit. Heart Dis. *6*, 41–47. https://doi.org/10.1111/j.1747-0803.2010.00465.x.
4. Wilkinson, J.D., Lowe, A.M., Salbert, B.A., Sleeper, L.A., Colan, S.D., Cox, G.F., Towbin, J.A., Connuck, D.M., Messere, J.E., and Lipshultz, S.E. (2012). Outcomes in children with Noonan syndrome and hypertrophic cardiomyopathy: a study from the Pediatric Cardiomyopathy Registry. Am. Heart J. *164*, 442–448. https://doi.org/10.1016/j.ahj.2012.04.018.
5. Aoki, Y., Niihori, T., Inoue, S.i., and Matsubara, Y. (2016). Recent advances in RASopathies. J. Hum. Genet. *61*, 33–39. https://doi.org/10.1038/jhg.2015.114.
6. Leoni, C., Blandino, R., Delogu, A.B., De Rosa, G., Onesimo, R., Verusio, V., Marino, M.V., Lanza, G.A., Rigante, D., Tartaglia, M., and Zampino, G. (2022). Genotype-cardiac phenotype correlations in a large single-center cohort of patients affected by RASopathies: Clinical implications and literature review. Am. J. Med. Genet. *188*, 431–445. https://doi.org/10.1002/ajmg.a.62529.
7. Johnston, J.J., van der Smagt, J.J., Rosenfeld, J.A., Pagnamenta, A.T., Alswaid, A., Baker, E.H., Blair, E., Borck, G., Brinkmann, J., Craigen, W., et al. (2018). Autosomal recessive Noonan syndrome associated with biallelic LZTR1 variants. Genet. Med. *20*, 1175–1185. https://doi.org/10.1038/gim.2017.249.
8. Bigenzahn, J.W., Collu, G.M., Kartnig, F., Pieraks, M., Vladimer, G.I., Heinz, L.X., Sedlyarov, V., Schischlik, F., Fauster, A., Rebsamen, M., et al. (2018). LZTR1 is a regulator of RAS ubiquitination and signaling. Science *362*, 1171–1177. https://doi.org/10.1126/science.aap8210.
9. Castel, P., Cheng, A., Cuevas-Navarro, A., Everman, D.B., Papageorge, A.G., Simanshu, D.K., Tankka, A., Galeas, J., Urisman, A., and McCormick, F. (2019). RIT1 oncoproteins escape LZTR1-mediated proteolysis. Science *363*, 1226–1230. https://doi.org/10.1126/science.aav1444.
10. Hanses, U., Kleinsorge, M., Roos, L., Yigit, G., Li, Y., Barbarics, B., El-Battrawy, I., Lan, H., Tiburcy, M., Hindmarsh, R., et al. (2020). Intronic CRISPR Repair in a Preclinical Model of Noonan Syndrome-Associated Cardiomyopathy. Circulation *142*, 1059–1076. https://doi.org/10.1161/CIRCULATIONAHA.119.044794.
11. Motta, M., Fidan, M., Bellacchio, E., Pantaleoni, F., Schneider-Heieck, K., Coppola, S., Borck, G., Salviati, L., Zenker, M., Cirstea, I.C., and Tartaglia, M. (2019). Dominant Noonan syndrome-causing LZTR1 mutations specifically affect the Kelch domain substrate-recognition surface and enhance RAS-MAPK signaling. Hum. Mol. Genet. *28*, 1007–1022. https://doi.org/10.1093/hmg/ddy412.
12. Sayed, N., Liu, C., and Wu, J.C. (2016). Translation of Human-Induced Pluripotent Stem Cells: From Clinical Trial in a Dish to Precision Medicine. J. Am. Coll. Cardiol. *67*, 2161–2176. https://doi.org/10.1016/j.jacc.2016.01.083.
13. van Mil, A., Balk, G.M., Neef, K., Buikema, J.W., Asselbergs, F.W., Wu, S.M., Doevendans, P.A., and Sluijter, J.P.G. (2018). Modelling inherited cardiac disease using human induced pluripotent stem cell-derived cardiomyocytes: progress, pitfalls, and potential. Cardiovasc. Res. *114*, 1828–1842. https://doi.org/10.1093/cvr/cvy208.
14. Meier, A.B., Raj Murthi, S., Rawat, H., Toepfer, C.N., Santamaria, G., Schmid, M., Mastantuono, E., Schwarzmayr, T., Berutti, R., Cleuziou, J., et al. (2022). Cell cycle defects underlie childhood-onset cardiomyopathy associated with Noonan syndrome. iScience *25*, 103596. https://doi.org/10.1016/j.isci.2021.103596.
15. Jaffré, F., Miller, C.L., Schänzer, A., Evans, T., Roberts, A.E., Hahn, A., and Kontaridis, M.I. (2019). Inducible Pluripotent Stem Cell-Derived Cardiomyocytes Reveal Aberrant Extracellular Regulated Kinase 5 and Mitogen-Activated Protein Kinase Kinase 1/2 Signaling Concomitantly Promote Hypertrophic Cardiomyopathy in RAF1-Associated Noonan Syndrome. Circulation *140*, 207–224. https://doi.org/10.1161/CIRCULATIONAHA.118.037227.
16. Josowitz, R., Mulero-Navarro, S., Rodriguez, N.A., Falce, C., Cohen, N., Ullian, E.M., Weiss, L.A., Rauen, K.A., Sobie, E.A., and Gelb, B.D. (2016). Autonomous and Non-autonomous Defects Underlie Hypertrophic Cardiomyopathy in BRAF-Mutant hiPSC-Derived Cardiomyocytes. Stem Cell Rep. *7*, 355–369. https://doi.org/10.1016/j.stemcr.2016.07.018.
17. Higgins, E.M., Bos, J.M., Dotzler, S.M., John Kim, C.S., and Ackerman, M.J. (2019). MRAS Variants Cause Cardiomyocyte Hypertrophy in Patient-Specific Induced Pluripotent Stem Cell-Derived Cardiomyocytes: Additional Evidence for MRAS as a Definitive Noonan Syndrome-Susceptibility Gene. Circ. Genom. Precis. Med. *12*, e002648. https://doi.org/10.1161/CIRCGEN.119.002648.
18. Knauer, C., Haltern, H., Schoger, E., Kügler, S., Roos, L., Zelarayán, L.C., Hasenfuss, G., Zimmermann, W.-H., Wollnik, B., and Cyganek, L. (2024). Preclinical evaluation of CRISPR-based therapies for Noonan syndrome caused by deep-intronic LZTR1 variants. Mol. Ther. Nucleic Acids *35*, 102123. https://doi.org/10.1016/j.omtn.2024.102123.
19. Kleinsorge, M., and Cyganek, L. (2020). Subtype-Directed Differentiation of Human iPSCs into Atrial and Ventricular Cardiomyocytes. STAR Protoc. *1*, 100026. https://doi.org/10.1016/j.xpro.2020.100026.
20. Kudo, T., Jeknić, S., Macklin, D.N., Akhter, S., Hughey, J.J., Regot, S., and Covert, M.W. (2018). Live-cell measurements of kinase activity in single cells using translocation reporters. Nat. Protoc. *13*, 155–169. https://doi.org/10.1038/nprot.2017.128.
21. Lemcke, H., Skorska, A., Lang, C.I., Johann, L., and David, R. (2020). Quantitative Evaluation of the Sarcomere Network of Human hiPSC-Derived Cardiomyocytes Using Single-Molecule Localization Microscopy. Int. J. Mol. Sci. *21*, 2819. https://doi.org/10.3390/ijms21082819.
22. Mosqueira, D., Mannhardt, I., Bhagwan, J.R., Lis-Slimak, K., Katili, P., Scott, E., Hassan, M., Prondzynski, M., Harmer, S.C., Tinker, A., et al. (2018). CRISPR/Cas9 editing in human pluripotent stem cell-cardiomyocytes highlights arrhythmias, hypocontractility, and energy depletion as potential therapeutic targets for hypertrophic cardiomyopathy. Eur. Heart J. *39*, 3879–3892. https://doi.org/10.1093/eurheartj/ehy249.
23. Levin, M.D., Saitta, S.C., Gripp, K.W., Wenger, T.L., Ganesh, J., Kalish, J.M., Epstein, M.R., Smith, R., Czosek, R.J., Ware, S.M., et al. (2018). Non-reentrant atrial tachycardia occurs independently of hypertrophic cardiomyopathy in RASopathy patients. Am. J. Med. Genet. *176*, 1711–1722. https://doi.org/10.1002/ajmg.a.38854.
24. Maron, B.J., Desai, M.Y., Nishimura, R.A., Spirito, P., Rakowski, H., Towbin, J.A., Rowin, E.J., Maron, M.S., and Sherrid, M.V. (2022). Diagnosis and Evaluation of Hypertrophic Cardiomyopathy: JACC State-of-the-Art Review. J. Am. Coll. Cardiol. *79*, 372–389. https://doi.org/10.1016/j.jacc.2021.12.002.

25. Cyganek, L., Tiburcy, M., Sekeres, K., Gerstenberg, K., Bohnenberger, H., Lenz, C., Henze, S., Stauske, M., Salinas, G., Zimmermann, W.-H., et al. (2018). Deep phenotyping of human induced pluripotent stem cell-derived atrial and ventricular cardiomyocytes. JCI Insight *3*, 99941. https://doi.org/10.1172/jci.insight.99941.

26. Tiburcy, M., Meyer, T., Liaw, N.Y., and Zimmermann, W.-H. (2020). Generation of Engineered Human Myocardium in a Multi-well Format. STAR Protoc. *1*, 100032. https://doi.org/10.1016/j.xpro.2020.100032.

27. NSEuroNet.com. https://nseuronet.com/php/. Accessed December 29, 2022.

28. Abe, T., Umeki, I., Kanno, S.-I., Inoue, S.I., Niihori, T., and Aoki, Y. (2020). LZTR1 facilitates polyubiquitination and degradation of RAS-GTPases. Cell Death Differ. *27*, 1023–1035. https://doi.org/10.1038/s41418-019-0395-5.

29. Canning, P., Cooper, C.D.O., Krojer, T., Murray, J.W., Pike, A.C.W., Chaikuad, A., Keates, T., Thangaratnarajah, C., Hojzan, V., Marsden, B.D., et al. (2013). Structural basis for Cul3 protein assembly with the BTB-Kelch family of E3 ubiquitin ligases. J. Biol. Chem. *288*, 7803–7814. https://doi.org/10.1074/jbc.M112.437996.

30. Mirdita, M., Schütze, K., Moriwaki, Y., Heo, L., Ovchinnikov, S., and Steinegger, M. (2022). ColabFold: making protein folding accessible to all. Nat. Methods *19*, 679–682. https://doi.org/10.1038/s41592-022-01488-1.

31. Steklov, M., Pandolfi, S., Baietti, M.F., Batiuk, A., Carai, P., Najm, P., Zhang, M., Jang, H., Renzi, F., Cai, Y., et al. (2018). Mutations in LZTR1 drive human disease by dysregulating RAS ubiquitination. Science *362*, 1177–1182. https://doi.org/10.1126/science.aap7607.

32. Cuevas-Navarro, A., Rodriguez-Muñoz, L., Grego-Bessa, J., Cheng, A., Rauen, K.A., Urisman, A., McCormick, F., Jimenez, G., and Castel, P. (2022). Cross-species analysis of LZTR1 loss-of-function mutants demonstrates dependency to RIT1 orthologs. Elife *11*, e76495. https://doi.org/10.7554/eLife.76495.

33. Nakamura, M., and Sadoshima, J. (2018). Mechanisms of physiological and pathological cardiac hypertrophy. Nat. Rev. Cardiol. *15*, 387–407. https://doi.org/10.1038/s41569-018-0007-y.

34. Nakhaei-Rad, S., Bazgir, F., Dahlmann, J., Busley, A.V., Buchholzer, M., Haghighi, F., Schänzer, A., Hahn, A., Kötter, S., Schanze, D., et al. (2022). Alteration of myocardial structure and function in RAF1-associated Noonan syndrome: Insights from cardiac disease modeling based on patient-derived iPSCs. Preprint at bioRxiv. https://doi.org/10.1101/2022.01.22.477319.

35. Wang, Y., Zhang, J., Zhang, P., Zhao, Z., Huang, Q., Yun, D., Chen, J., Chen, H., Wang, C., and Lu, D. (2020). LZTR1 inactivation promotes MAPK/ERK pathway activation in glioblastoma by stabilizing oncoprotein RIT1. Preprint at bioRxiv. https://doi.org/10.1101/2020.03.14.989954.

36. Marzahn, M.R., Marada, S., Lee, J., Nourse, A., Kenrick, S., Zhao, H., Ben-Nissan, G., Kolaitis, R.-M., Peters, J.L., Pounds, S., et al. (2016). Higher-order oligomerization promotes localization of SPOP to liquid nuclear speckles. EMBO J. *35*, 1254–1275. https://doi.org/10.15252/embj.201593169.

37. Karbassi, E., Fenix, A., Marchiano, S., Muraoka, N., Nakamura, K., Yang, X., and Murry, C.E. (2020). Cardiomyocyte maturation: advances in knowledge and implications for regenerative medicine. Nat. Rev. Cardiol. *17*, 341–359. https://doi.org/10.1038/s41569-019-0331-x.

38. Guo, Y., and Pu, W.T. (2020). Cardiomyocyte Maturation: New Phase in Development. Circ. Res. *126*, 1086–1106. https://doi.org/10.1161/CIRCRESAHA.119.315862.

39. Rössler, U., Hennig, A.F., Stelzer, N., Bose, S., Kopp, J., Søe, K., Cyganek, L., Zifarelli, G., Ali, S., von der Hagen, M., et al. (2021). Efficient generation of osteoclasts from human induced pluripotent stem cells and functional investigations of lethal CLCN7-related osteopetrosis. J. Bone Miner. Res. *36*, 1621–1635. https://doi.org/10.1002/jbmr.4322.

40. Yousefi, R., Fornasiero, E.F., Cyganek, L., Montoya, J., Jakobs, S., Rizzoli, S.O., Rehling, P., and Pacheu-Grau, D. (2021). Monitoring mitochondrial translation in living cells. EMBO Rep. *22*, e51635. https://doi.org/10.15252/embr.202051635.

41. Schmidt, U., Weigert, M., Broaddus, C., and Myers, G. (2018). Cell Detection with Star-Convex Polygons. In Cell Detection with Star-Convex Polygons, A.F. Frangi, J.A. Schnabel, C. Davatzikos, C. Alberola-López, and G. Fichtinger, eds. (Cham: Springer International Publishing), pp. 265–273.

42. Haeussler, M., Schönig, K., Eckert, H., Eschstruth, A., Mianné, J., Renaud, J.-B., Schneider-Maunoury, S., Shkumatava, A., Teboul, L., Kent, J., et al. (2016). Evaluation of off-target and on-target scoring algorithms and integration into the guide RNA selection tool CRISPOR. Genome Biol. *17*, 148. https://doi.org/10.1186/s13059-016-1012-2.

43. Ahlers, J., Althviz Moré, D., Amsalem, O., Anderson, A., Bokota, G., Boone, P., Bragantini, J., Buckley, G., Burt, A., Bussonnier, M., et al. (2023). Napari: A Multi-Dimensional Image Viewer for Python. Zenodo.

44. Zech, A.T.L., Prondzynski, M., Singh, S.R., Pietsch, N., Orthey, E., Alizoti, E., Busch, J., Madsen, A., Behrens, C.S., Meyer-Jens, M., et al. (2022). ACTN2 Mutant Causes Proteopathy in Human iPSC-Derived Cardiomyocytes. Cells *11*, 2745. https://doi.org/10.3390/cells11172745.

45. Suomi, T., and Elo, L.L. (2017). Enhanced differential expression statistics for data-independent acquisition proteomics. Sci. Rep. *7*, 5869. https://doi.org/10.1038/s41598-017-05949-y.

46. Seyednasrollah, F., Rantanen, K., Jaakkola, P., and Elo, L.L. (2016). ROTS: reproducible RNA-seq biomarker detector-prognostic markers for clear cell renal cell cancer. Nucleic Acids Res. *44*, e1. https://doi.org/10.1093/nar/gkv806.

47. Bindea, G., Mlecnik, B., Hackl, H., Charoentong, P., Tosolini, M., Kirilovsky, A., Fridman, W.-H., Pagès, F., Trajanoski, Z., and Galon, J. (2009). ClueGO: a Cytoscape plug-in to decipher functionally grouped gene ontology and pathway annotation networks. Bioinformatics *25*, 1091–1093. https://doi.org/10.1093/bioinformatics/btp101.

48. Pasqualin, C., Gannier, F., Yu, A., Malécot, C.O., Bredeloux, P., and Maupoil, V. (2016). SarcOptiM for ImageJ: high-frequency online sarcomere length computing on stimulated cardiomyocytes. Am. J. Physiol. Cell Physiol. *311*, C277–C283. https://doi.org/10.1152/ajpcell.00094.2016.

49. Nacak, T.G., Leptien, K., Fellner, D., Augustin, H.G., and Kroll, J. (2006). The BTB-kelch protein LZTR-1 is a novel Golgi protein that is degraded upon induction of apoptosis. J. Biol. Chem. *281*, 5065–5071. https://doi.org/10.1074/jbc.M509073200.

50. Eberth, A., and Ahmadian, M.R. (2009). In vitro GEF and GAP assays. Curr. Protoc. Cell Biol. *14*, Unit 14.9. https://doi.org/10.1002/0471143030.cb1409s43.

51. Evans, R., O'Neill, M., Pritzel, A., Antropova, N., Senior, A., Green, T., Žídek, A., Bates, R., Blackwell, S., Yim, J., et al. (2021). Protein Complex Prediction with AlphaFold-Multimer. Preprint at bioRxiv. https://doi.org/10.1101/2021.10.04.463034.

STAR★METHODS

KEY RESOURCES TABLE

REAGENT or RESOURCE	SOURCE	IDENTIFIER
Antibodies		
α-actinin monoclonal mouse	Sigma-Aldrich	RRID: AB_476766
Alexa 488 polyclonal goat anti-rabbit	Thermo Fisher Scientific	RRID: AB_143165
Alexa 555 polyclonal donkey anti-mouse	Thermo Fisher Scientific	RRID: AB_2536180
FLAG monoclonal mouse	Sigma-Aldrich	RRID: AB_262044
HA monoclonal rabbit	Cell Signaling	RRID: AB_1549585
His monoclonal rabbit	Thermo Fisher Scientific	RRID: AB_2810125
LZTR1 monoclonal rabbit	Abcam	RRID: AB_3076250
MLC2V polyclonal rabbit	Proteintech	RRID: AB_2147453
MRAS polyclonal rabbit	Proteintech	RRID: AB_10950895
MYC monoclonal mouse	Cell Signaling	RRID: AB_331783
NANOG monoclonal mouse	Thermo Fisher Scientific	RRID: AB_2536677
OCT3/4-PE monoclonal human	Miltenyi Biotec	RRID: AB_2784442
pan-RAS monoclonal mouse	Merck Millipore	RRID: AB_2121151
RIT1 polyclonal rabbit	Abcam	RRID: AB_882379
TRA-1-60 monoclonal mouse	Abcam	RRID: AB_778563
TRA-1-60-Alexa488 monoclonal mouse	BD Biosciences	RRID: AB_1645379
Vinculin monoclonal mouse	Sigma-Aldrich	RRID: AB_477629
HRP polyclonal donkey anti-rabbit	Sigma-Aldrich	RRID: AB_2722659
HRP polyclonal donkey anti-mouse	Sigma-Aldrich	RRID: AB_772210
Chemicals, peptides, and recombinant proteins		
Fetal bovine serum	Thermo Fisher Scientific	Cat# 10500-064
JNK-IN-8	Hycultec	Cat# HY-13319
MG-132	InvivoGen	Cat# tlrl-mg132-2
Pevonedistat (MLN49249)	Hycultec	Cat# HY-70062
Trametinib	Selleck Chemicals	Cat# S2673
Critical commercial assays		
BCA assay kit	Thermo Fisher Scientific	Cat# 23225
NucleoBond Xtra Midi Plus EF kit	Macherey-Nagel	Cat# 740410.50
ROX passive dye	Bio-Rad	Cat# 1725858
SureSelect Human All Exon V6 kit	Agilent	N/A
SYBR green PCR master mix	Bio-Rad	Cat# 1708880
Deposited data		
Mass spectrometry proteomics	This paper	ProteomeXchange: PXD038425 and PXD038417
Experimental models: Cell lines		
Human iPSC line: WT1	Rössler et al.[39]	UMGi014-C clone 14
Human iPSC line: WT11	Yousefi et al.[40]	UMGi130-A clone 8
Human iPSC line: LZTR1^{KO}	Hanses et al.[10]	UMGi030-A clone 14
Human iPSC line: LZTR1^{L580P}	This paper	UMGi137-A clone 2
Human iPSC line: L580P$^{corr\text{-}het}$	This paper	UMGi137-A-1 clone D8
Human iPSC line: L580P$^{corr\text{-}hom}$	This paper	UMGi137-A-1 clone D1
Human foreskin fibroblasts: HFF-1	ATCC	Cat# SCRC-1041
Expi-293F	Thermo Fisher Scientific	Cat# A14527

(*Continued on next page*)

Continued		
REAGENT or RESOURCE	SOURCE	IDENTIFIER
HEK293T	ATCC	Cat# CRL-11268
Oligonucleotides		
Primers used in this study see Table S2	This paper	N/A
Recombinant DNA		
Plasmids used in this study see Table S3	This paper	N/A
Software and algorithms		
CellPathfinder	Yokogawa Electric Corporation	https://www.yokogawa.com/de/library/documents-downloads/software/lsc-cellpathfinder-software/
CellProfiler	BROAD institute	https://www.broadinstitute.org/publications/broad339241
ColabFold (version 02c53)	Mirdita et al.[30]	https://colab.research.google.com/github/sokrypton/ColabFold/blob/main/AlphaFold2.ipynb
CRISPOR	Tefor infrastructure	http://crispor.tefor.net/
CytoSolver	IonOptix	https://www.ionoptix.com/products/software/cytosolver-transient-analysis-tool/
GenomeStudio v2.0	Illumina	https://support.illumina.com/downloads/genomestudio-2-0.html
ImageJ	NIH	https://imagej.net/ij/
ImageLab	BioRad	https://www.bio-rad.com/de-de/product/image-lab-software?ID=KRE6P5E8Z
LabChart	ADInstruments	https://www.adinstruments.com/products/labchart
MATLAB	MathWorks	https://www.mathworks.com/
Prism 10	GraphPad	https://www.graphpad.com/scientific-software/prism
Spectronaut software	Biognosys	https://biognosys.com/software/spectrodive
StarDist	Schmidt et al.[41]	https://stardist.net/
Varbank 2.0	Cologne Center for Genomics (CCG)	https://varbank.ccg.uni-koeln.de/
Other		
Axio Imager M2 microscope	Carl Zeiss	N/A
CASY cell count system	OMNI Life Science	N/A
Cytomotion Lite system	IonOptix	N/A
CQ1 confocal image cytometer	Yokogawa Electric Corporation	N/A
MutationTaster		https://www.mutationtaster.org/
PolyPhen-2		http://genetics.bwh.harvard.edu/pph2/
SIFT		https://sift.bii.a-star.edu.sg/

RESOURCE AVAILABILITY

Lead contact

Further information and requests for resources and reagents should be directed to and will be fulfilled by the lead contact, Lukas Cyganek (lukas.cyganek@gwdg.de).

Materials availability

All human iPSC lines used in this study are deposited in the stem cell biobank of the University Medical Center Göttingen and are available for research use upon request. Requests of material, including iPSC lines and plasmids, can be directed to and will be fulfilled by the lead contact. Reagents and cell lines can be transferred after the completion of a materials transfer agreement.

Data and code availability

- The mass spectrometry proteomics datasets are available at the ProteomeXchange Consortium via the PRIDE partner repository (https://www.proteomexchange.org/) with the identifiers PXD038425 and PXD038417.
- This paper does not report original code.
- Any additional information required to reanalyze the data reported in this paper is available from the lead contact upon request.

EXPERIMENTAL MODEL AND STUDY PARTICIPANT DETAILS

Human iPSC lines

Human iPSC lines from two healthy donors (UMGi014-C clone 14 and UMGi130-A clone 8), from one NS patient with biallelic truncating variants in *LZTR1* (UMGi030-A clone 14), from one NS patient with a pathological missense variant in *LZTR1* (UMGi137-A clone 2), as well as heterozygous and homozygous CRISPR/Cas9-corrected iPSC lines (UMGi137-A-1 clone D8 and UMGi137-A-1 clone D1) were used in this study. Details on reprogramming and CRISPR/Cas9 editing are provided in the method details below.

Ethical approval

The study was approved by the Ethics Committee of the University Medical Center Göttingen (approval number: 10/9/15) and carried out in accordance with the approved guidelines. Written informed consent was obtained from all participants or their legal representatives prior to the participation in the study.

METHOD DETAILS

Whole exome sequencing

Whole exome sequencing on genomic DNA of the patient was performed using the SureSelect Human All Exon V6 kit (Agilent) on an Illumina HiSeq 4000 sequencer. The "Varbank 2.0" pipeline of the Cologne Center for Genomics (CCG) was used to analyze and interpret the exome data, as previously described.[10] Co-segregation analysis was performed in the family. Computational predictions for the pathogenicity of the variant were performed using MutationTaster (https://www.mutationtaster.org/), SIFT (https://sift.bii.a-star.edu.sg/), and PolyPhen-2 (http://genetics.bwh.harvard.edu/pph2/).

Generation and culture of human iPSCs

Human iPSC lines from two healthy donors, from one NS patient with biallelic truncating variants in *LZTR1* (NM_006767.4: c.27dupG/p.Q10Afs*24, c.1943-256C>T/p.T648fs*36), from one NS patient with a pathological missense variant in *LZTR1* (NM_006767.4: c.1739T>C/p.L580P; ClinVar: RCV000677201.1), as well as heterozygous and homozygous CRISPR/Cas9-corrected iPSC lines were used in this study. Wild type iPSC lines UMGi014-C clone 14 (isWT1.14, here abbreviated as WT1) and UMGi130-A clone 8 (isWT11.8, here abbreviated as WT11) were generated from dermal fibroblasts and peripheral blood mononuclear cells from two male donors, respectively, using the integration-free Sendai virus and described previously.[39,40] Patient-specific iPSC line UMGi030-A clone 14 (isHOCMx1.14, here abbreviated as $LZTR1^{KO}$) was generated from patient's dermal fibroblasts using the integration-free Sendai virus and described previously.[10] Patient-specific iPSC line UMGi137-A clone 2 (isNoonSf1.2, here abbreviated as $LZTR1^{L580P}$) was generated from patient's dermal fibroblasts using the integration-free Sendai virus according manufacturer's instructions with modifications, as previously described.[10] Genetic correction of the pathological gene variant in the patient-derived iPSC line UMGi137-A clone 2 was performed using ribonucleoprotein-based CRISPR/Cas9 using crRNA/tracrRNA and Hifi SpCas9 (IDT DNA technologies) by targeting exon 15 of the *LZTR1* gene, as previously described.[10] The guide RNA target sequence was (PAM in bold): 5′-GCGGCACTCTCGCACACAAC **CGG**-3'. For homology-directed repair, a single-stranded oligonucleotide with 45-bp homology arms was used. After automated clonal singularization using the single cell dispenser CellenOne (Cellenion/Scienion) in StemFlex medium (Thermo Fisher Scientific), successful genome editing was identified by Sanger sequencing and the CRISPR-corrected isogenic iPSC lines UMGi137-A-1 clone D8 (isNoonSf1-corr.D8, here abbreviated as $L580P^{corr\text{-}het}$) and UMGi137-A-1 clone D1 (isNoonSf1-corr.D1, here abbreviated as $L580P^{corr\text{-}hom}$) were established. Newly generated iPSC lines were maintained on Matrigel-coated (growth factor reduced, BD Biosciences) plates, passaged every 4–6 days with Versene solution (Thermo Fisher Scientific) and cultured in StemMACS iPS-Brew XF medium (Miltenyi Biotec) supplemented with 2 μM Thiazovivin (Merck Millipore) on the first day after passaging with daily medium change for at least ten passages before being used for molecular karyotyping, pluripotency characterization, and differentiation experiments. Pluripotency analysis via immunocytochemistry and flow cytometry was performed, as previously described.[10] For molecular karyotyping, genomic DNA of iPSC clones was sent for genome-wide analysis via Illumina BeadArray (Life&Brain, Germany). Digital karyotypes were analyzed in GenomeStudio v2.0 software (Illumina). For off-target screening, the top five predicted off-target regions for the respective guide RNA ranked by the CFD off-target score using CRISPOR[42] were analyzed by Sanger sequencing. Human iPSCs and iPSC-derivatives were cultured in feeder-free and serum-free culture conditions in a humidified incubator at 37°C and 5% CO_2.

Cardiomyocyte differentiation of iPSCs and generation of engineered heart muscle

Human iPSC lines were differentiated into ventricular iPSC-CMs via WNT signaling modulation and subsequent metabolic selection, as previously described,[19] and cultivated in feeder-free and serum-free culture conditions until day 60 post-differentiation before being used for molecular and cellular experiments. Defined, serum-free EHMs were generated from iPSC-CMs around day 30 of differentiation and human foreskin fibroblasts (ATCC) at a 70:30 ratio according to previously published protocols.[26] Optical analysis of contractility and rhythm of spontaneously beating EHMs in a 48 well plate (myrPlate TM5, myriamed GmbH) was performed between day 34 and day 42 of culture using a custom-built setup with a high-speed camera by recording the movement of the two UV light-absorbing flexible poles. Contractility parameters of EHM recordings of at least 1 min recording time were analyzed via a custom-build script in MATLAB (MathWorks). For each iPSC line, three individual differentiations were used for EHM casting.

Biosensor-based analysis of ERK signaling dynamics in iPSC-CMs

In brief, the ERK kinase translocation reporter (ERK-KTR) biosensor consists of an ERK-specific docking site, a nuclear localization signal (NLS), a nuclear export signal (NES), and mClover. Endogenous, phosphorylated ERK binds to the biosensor and phosphorylates its NLS and NES resulting in a nucleus-cytoplasm shuttling according to ERK activity.[20] ERK-KTR biosensor encoding lentiviral particles were produced in HEK293T cells transfected with transfer, envelope, and packaging plasmids using Lipofectamine 3000 (Thermo Fisher Scientific) according to manufacturer's instructions. pLentiPGK Puro DEST ERKKTRClover was a gift from Markus Covert (RRID:Addgene_90227), pMD2.G was a gift from Didier Trono (RRID:Addgene_12259), and psPAX2 was a gift from Didier Trono (RRID:Addgene_12260). Virus was harvested from day 2 to day 5 post-transfection by medium collection and centrifugation at 500×g at 4°C for 5 min. The harvested virus was filtered using a 0.45 μm filter and a syringe. For transduction, 15,000 iPSC-CMs were seeded per well of a 96-well plate and lentiviral transduction was performed 7 days after cell digestion. Lentivirus was diluted in culture medium supplemented with 100 U/ml penicillin, 100 μg/mL streptomycin (Thermo Fisher Scientific), and 10 μg/mL Polybrene Transfection Reagent (Merck). After 24 h of incubation, medium was replaced with cardio culture medium and cells were maintained for additional 7 days. For live-cell imaging, biosensor-transduced iPSC-CM cultures at day 60 of differentiation were treated with 100 nM MEK inhibitor trametinib (Selleck Chemicals), 100 nM JNK inhibitor JNK-IN-8 (Hycultec), or 1:1,000 DMSO (Sigma-Aldrich) for 60 min, before stimulation with 10% fetal bovine serum for another 60 min. Cells were imaged every 10 min for a total time of 120 min. Live cell imaging experiments were acquired using the CQ1 confocal image cytometer (Yokogawa Electric Corporation) and CellPathfinder software (Yokogawa Electric Corporation) under environmental control (37°C, 5% CO_2). Exported images were processed using the StarDist method for nucleus segmentation.[41] The StarDist network was retrained on 60 images from our dataset with annotations manually produced with napari.[43] For a new image, the nuclei were then segmented with StarDist, and a ring element around each nucleus was computed to approximate the cytosol. The mean fluorescence intensity of both compartments was measured for each cell individually.

Proteomics and Western blot analysis of iPSC-CMs

For proteomic analysis, iPSC-CMs were pelleted at day 60 of differentiation by scratching in RIPA buffer (Thermo Fisher Scientific) containing phosphatase and protease inhibitor (Thermo Fisher Scientific) and snap-frozen in liquid nitrogen. Cell pellets were reconstituted in 8 M urea/2 M thiourea solution (Sigma-Aldrich) and lysed by five freeze-thaw cycles at 30°C and 1.600 rpm. Protein containing supernatant was collected by centrifugation. Nucleic acid was degraded enzymatically with 0.125 U/μg benzonase (Sigma-Aldrich), and protein concentration was determined by Bradford assay (Bio-Rad). Five μg protein was processed for LC-MS/MS analysis, as previously described.[44] Briefly, protein was reduced (2.5 mM dithiothreitol, Sigma-Aldrich; 30 min at 37°C) and alkylated (10 mM iodacetamide, Sigma-Aldrich; 15 min at 37°C) before proteolytic digestion with LysC (enzyme to protein ratio 1:100, Promega) for 3 h and with trypsin (1:25, Promega) for 16 h both at 37°C. The reaction was stopped with 1% acetic acid (Sigma-Aldrich), and the peptide mixtures were desalted on C-18 reverse phase material (ZipTip μ-C18, Millipore). Eluted peptides were concentrated by evaporation under vacuum and subsequently resolved in 0.1% acetic acid/2% acetonitrile containing HRM/iRT peptides (Biognosys) according to manufacturer's recommendation. LC-MS/MS analysis was performed in data-independent acquisition (DIA) mode using an Ultimate 3000 UPLC system coupled to an Exploris 480 mass spectrometer (Thermo Scientific). Peptides were separated on a 25 cm Accucore column (75 μm inner diameter, 2.6 μm, 150 A, C18) at a flow rate of 300 nL/min in a linear gradient for 60 min. Spectronaut software (Biognosys) was used for the analysis of mass spectrometric raw data. For peptide and protein identification, the Direct DIA approach based on UniProt database limited to human entries was applied. Carbamidomethylation at cysteine was set as static modification, oxidation at methionine and protein N-terminal acetylation were defined as variable modifications, and up to two missed cleavages were allowed. Ion values were parsed when at least 20% of the samples contained high quality measured values. Peptides were assigned to protein groups and protein inference was resolved by the automatic workflow implemented in Spectronaut. Statistical data analysis was conducted using an in-house developed R tool and based on median-normalized ion peak area intensities. Methionine oxidized peptides were removed before quantification. Differential abundant proteins (p-value ≤ 0.05) were identified by the algorithm ROPECA[45] and application of the reproducibility-optimized peptide change averaging approach[46] applied on peptide level. Only proteins quantified by at least two peptides were considered for further analysis. Reactome pathway enrichment analysis was performed using the ClueGo plugin in Cytoscape.[47] For each iPSC line, at least three individual differentiations were analyzed. For Western blot analysis, protein containing supernatant was collected by centrifugation. Protein concentration was determined by BCA assay (Thermo Fisher Scientific). Samples were denatured at 95°C for 5 min 15 μg

protein were loaded onto a 4–15% Mini-PROTEAN TGX Stain-Free precast gel (Bio-Rad). The protein was separated by sodium dodecyl sulfate-polyacrylamide gel electrophoresis (SDS-PAGE) by applying 200 V for 30 min. Post-running, TGX gels were activated via UV light application using the Trans-Blot Turbo transfer system (Bio-Rad). While blotting, proteins were transferred to a nitrocellulose membrane (25 V constant, 1.3 A for 7 min). Total protein amount was detected via the ChemiDoc XRS+ (Bio-Rad) system and used for protein normalization. After 1 h in blocking solution (5% milk in TBS-T, Sigma-Aldrich), membranes were incubated in primary antibody solution (1% milk in TBS-T) overnight. Membrane was washed trice with TBS-T before applying the secondary antibody (1:10,000 in 1% milk in TBS-T) at RT for 1 h. After washing, signals were detected upon application of SuperSignal West Femto Maximum Sensitivity Substrat (Thermo Fisher Scientific). Image acquisition was performed with the ChemiDoc XRS+ (Bio-Rad) at the high-resolution mode. For protein quantification, ImageLab (Bio-Rad) was used and protein levels were first normalized to total protein and second to the corresponding WT samples on each blot. For ERK signaling analysis, iPSC-CMs at day 60 of differentiation were treated with 10 nM trametinib (Selleck Chemicals) for 30 min and stimulated with 10% fetal bovine serum (Thermo Fisher Scientific). For analysis of degradation pathways, iPSC-CMs at day 60 of differentiation were treated with 1–2 μM pevonedistat (Hycultec) or 750 nM MG-132 (InvivoGen) for three days. For each iPSC line, at least three individual differentiations/conditions were analyzed.

Real-time PCR analysis of iPSC-CMs

Pellets of iPSC-CMs at day 60 of differentiation were snap-frozen in liquid nitrogen and stored at −80°C. Total RNA was isolated using the NucleoSpin RNA Mini kit (Macherey-Nagel) according to manufacturer's instructions. 200 ng RNA was used for the first-strand cDNA synthesis by using the MULV Reverse Transcriptase and Oligo d(T)16 (Thermo Fisher Scientific). For real-time PCR, cDNA was diluted 1:1 with nuclease-free water (Promega). Quantitative real-time PCR reactions were carried out using the SYBR Green PCR master mix and ROX Passive Reference Dye (Bio-Rad) with Micro-Amp Optical 384-well plates, and the 7900HT fast real-time PCR system (Applied Biosystems) according to the manufacturer's instructions with the following parameters: 95°C for 10 min, followed by 40 cycles at 95°C for 15 s and 60°C for 1 min. Analysis was conducted using the ΔΔCT method and values were normalized to *GAPDH* gene expression and to WT controls. Primer sequences are listed in Table S2 in the supplement.

Analysis of sarcomere length and myofibril organization of iPSC-CMs

To analyze the sarcomere length and myofibril organization, iPSC-CMs were cultured on Matrigel-coated coverslips and fixed at day 60 of differentiation in 4% Roti-Histofix (Carl Roth) at RT for 10 min and blocked with 1% Bovine Serum Albumin (BSA; Sigma-Aldrich) in PBS (Thermo Fisher Scientific) overnight at 4°C. Primary antibodies were applied in 1% BSA and 0.1% Triton X-100 (Carl Roth) in PBS at 37°C for 1 h or at 4°C overnight. Secondary antibodies with minimal cross reactivity were administered in 1% BSA in PBS (Thermo Fisher Scientific) at RT for 1 h. Nuclei were stained with 8.1 μM Hoechst 33342 (Thermo Fisher Scientific) at RT for 10 min. Samples were mounted in Fluoromount-G (Thermo Fisher Scientific). Images were collected using the Axio Imager M2 microscopy system (Carl Zeiss) and Zen 2.3 software. For analysis of the sarcomere length, images with α-actinin staining of iPSC-CMs were evaluated using the SarcOptiM plugin in ImageJ (National Institutes of Health).[48] Here, three independent lines along different myofibrils within one cell were selected to calculate the mean sarcomere length per cell. For each iPSC line, three individual differentiations with 9–13 images per differentiation and two cells per image were analyzed. To analyze the myofibril organization, images with α-actinin staining of iPSC-CMs were processed using the Tubeness and Fast Fourier Transform plugins in ImageJ. Processed images were radially integrated using the Radial Profile Plot plugin in ImageJ and the relative amplitude of the first-order peak in the intensity profile as a measure of sarcomere and myofibril regularity was automatically analyzed using LabChart (ADInstruments). For each iPSC line, three individual differentiations with 7–11 images per differentiation were analyzed.

Analysis of cell size of iPSC-CMs

To study cellular hypertrophy, iPSC-CMs at day 60 of differentiation were analyzed for cell size in suspension, as previously described.[10] In brief, iPSC-CMs at day 50 of differentiation were plated at a density of 2.5×10^5 cells per well on Matrigel-coated 12-well plates. At day 60 of differentiation, cells were singularized with StemPro Accutase Cell Dissociation Reagent (Thermo Fisher Scientific) and measured for cell diameter using the CASY cell counter system (OMNI Life Science). Each value represents a mean of 5×10^2 to 1.5×10^4 cells per measurement. To exclude cell debris and cell clusters, only values within a diameter range of 15–40 μm were selected. For each iPSC line, at least three individual differentiations with 3–5 replicates per differentiation were analyzed. To study the effect of MEK inhibition on $LZTR1^{L580P}$ iPSC-CMs, cultured at a density of 6×10^5 cells per well were treated with 10 nM trametinib for 5 days before being measured via the CASY cell counter.

Video-based contractility analysis of iPSC-CMs

To analyze contractile parameters in monolayer, iPSC-CMs were cultured on Matrigel-coated 6-well plates and measured using the Cytomotion imaging setup (IonOptix). Recordings (60–75 s in duration) were acquired at 250 frames per second. Contractile parameters (beat frequency, beat regularity, contraction and relaxation time) were analyzed using CytoSolver.

Ectopic expression of LZTR1 variants in iPSC-CMs

For ectopic expression studies, the human WT *LZTR1* coding sequence was synthesized (Genewiz/Azenta Life Sciences) and subcloned in *pcDNA3-HA-humanNEMO* (gift from Kunliang Guan, Addgene plasmid #13512) by exchanging the *NEMO* coding sequence. Additionally, the HA-tag was exchanged by an FLAG tag by synthesis of the fragment and subcloning in *pcDNA3-HA-LZTR1-WT* (Genewiz/Azenta Life Sciences). Patient-specific mutations were introduced into *pcDNA3-HA-LZTR1-WT* and *pcDNA3-FLAG-LZTR1-WT* using mutagenesis PCR. Plasmid DNA was isolated via the endotoxin-free NucleoBond Xtra Midi Plus EF kit (Macherey-Nagel). For transfection, WT1 iPSC-CMs cultured on Matrigel-coated 4-well chamber slides at a density of 7×10^4 cells per well were transfected at day 60 of differentiation with the respective plasmids using Lipofectamine Stem Transfection Reagent (Thermo Fisher Scientific) according to manufacturer's instructions with 700 ng per plasmid. After 24 h post-transfection, cells were fixed, stained, and imaged as described above.

To quantitatively analyze speckle size and filament length, a custom-build pipeline in CellProfiler (BROAD institute) was applied. For each *LZTR1* variant, plasmid transfections were performed in at least three replicates. All plasmids used are listed in Table S3 in the supplement.

Expression and purification of recombinant LZTR1 proteins

$LZTR1^{WT}$ and $LZTR1^{L580P}$ were expressed as C-terminal His-tagged proteins in Expi-293F cells (Thermo Fisher Scientific). pcDNA3.1-LZTR1-Myc-6xHis plasmid was a gift from Jens Kroll (Heidelberg University and German Cancer Research Center (DKFZ-ZMBH Alliance)).[49] The $LZTR1^{L580P}$ variant was introduced into the plasmid by site-directed mutagenesis as previously described.[11] Cells were transfected using ExpiFectamine 293 Reagent (Thermo Fisher Scientific) and cultured at a density of $3\text{-}5\times10^6$ cells/ml in a 37°C incubator with ≥80% relative humidity and 8% CO2 on an orbital shaker at 125×g for 3–4 days. Expression of the recombinant LZTR1 proteins was confirmed by Western blot analysis using an anti-His tag monoclonal rabbit antibody (Thermo Fisher Scientific). Following confirmation of expression, cells were harvested and lysed in a buffer containing 50 mM Tris/HCl (pH 7.4), 250 mM NaCl, 5 mM $MgCl_2$, 0.5 mM CHAPS, 0.5 mM sodium deoxycholate, 1 mM Na_3VO_4, 1 mM NaF, and 5% glycerol, and one complete EDTA-free protease inhibitor mixture tablet (Roche Diagnostics). The lysates were centrifuged at 20,000×g for 30 min at 4°C to obtain the soluble protein fraction containing the expressed LZTR1 proteins. Soluble fractions were applied to a Ni-NTA resin column and bound proteins, including LZTR1 proteins, were eluted with a buffer containing 50 mM Tris/HCl (pH 7.4), 250 mM NaCl, 5 mM $MgCl_2$, 5% glycerol, and 250 mM imidazole. Purified LZTR1 proteins were concentrated using a 30 kDa MWCO concentrator (Amicon), snap-frozen in liquid nitrogen, and stored at −80°C.

Analytical size exclusion chromatography (SEC) of soluble recombinant LZTR1 proteins

Purified LZTR1 proteins were centrifuged at 12,000×g for 10 min before being applied to an analytical Superose 6 10/300 SEC column (GE Healthcare Life Sciences) using a buffer containing 50 mM Tris/HCl (pH 7.4), 250 mM NaCl, 5 mM $MgCl_2$, 0.5 mM CHAPS, 0.5 mM sodium deoxycholate, and 5% glycerol at a flow rate of 0.5 mL/min. The column was calibrated using a kit (GE Healthcare Life Sciences) containing standards of known molecular weight, including blue dextran (2000 kDa), thyroglobulin (669 kDa), ferritin (440 kDa), aldolase (158 kDa), and ovalbumin (44 kDa) at their respective concentrations. The proteins were eluted with the equilibration buffer at a constant flow rate and the absorbance at 260 nm was monitored with a UV detector. The elution profiles were analyzed using OriginPro 2021 software (OriginLab) to determine the retention volume and molecular weight of the $LZTR1^{WT}$ and $LZTR1^{L580P}$ proteins. To ensure the accuracy of the SEC results, trichloroacetic acid precipitation of the SEC fractions was performed. The precipitated proteins were visualized by SDS-PAGE and Western blot analysis using an anti-His tag monoclonal rabbit antibody (Thermo Fisher Scientific) to determine the protein distribution in each fraction.

Pull-down assay for analysis of LZTR1-RAS interactions

Recombinant GST-fused RAS proteins in both inactive (GDP-bound) and active (GppNHp-bound) states were prepared according to established protocols.[50] In brief, nucleotide and protein concentrations were determined using HPLC and Bradford reagents, and aliquots were stored at −80°C. His Mag Sepharose Ni beads (GE Healthcare) were used for the protein-protein interaction assay. Recombinant $LZTR1^{WT}$ and $LZTR1^{L580P}$ proteins were each mixed with MRAS and RIT1 proteins in a buffer containing 50 mM Tris/HCl (pH 7.4), 250 mM NaCl, 10 mM $MgCl_2$, 20 mM imidazole, and 5% glycerol. Individual protein mixtures were prepared for each LZTR1 variant and RAS protein combination. Input samples were collected for analysis, representing the initial protein composition. The remaining volume of each sample was subjected to pull-down using His Mag Sepharose Ni beads. Mixtures were incubated for 1 h at 4°C to allow for specific protein-protein interactions. After incubation, beads were thoroughly washed with binding buffer to remove non-specific binding. Protein complexes were eluted from the beads using a buffer containing 250 mM imidazole. Eluted samples were analyzed by SDS-PAGE to visualize the separated proteins. To confirm the interactions, Western blotting was performed using an anti-His tag monoclonal rabbit antibody (Thermo Fisher Scientific) and GST monoclonal mouse antibody (own antibody). GST control samples were included in each pull-down experiment to serve as negative controls, assessing the specificity of observed protein-protein interactions.

In silico prediction of protein structures and multimer complexes

Homo-trimer configurations of the different *LZTR1* variants and configurations of LZTR1 with cullin 3 and MRAS were predicted using ColabFold (version 02c53)[30] and AlphaFold-multimer v2[51] with 6 recycles and no templates on an A5000 GPU with 24 GBs of RAM and repeated twice. The five predicted models for each variant were ranked according to the predicted template modeling score and interactions between the chains were inspected through the predicted alignment error generated by AlphaFold-multimer.

QUANTIFICATION AND STATISTICAL ANALYSIS

Data are presented as the mean ± standard error of the mean, unless otherwise specified. Statistical comparisons were performed using the D'Agostino-Pearson normality test and the nonparametric Kruskal-Wallis test followed by Dunn correction or the parametric t test in Prism 10 (GraphPad). Results were considered statistically significant when the p-value was ≤ 0.05.